Ultrasonics Sonochemistry 100 (2023) 106624

Contents lists available at ScienceDirect

Ultrasonics Sonochemistry

journal homepage: www.elsevier.com/locate/ultson

Highly efficient ultrasound-driven Cu-MOF/$ZnWO_4$ heterostructure: An efficient visible-light photocatalyst with robust stability for complete degradation of tetracycline

Jenson Samraj Jeyaprakash [a], Manju Rajamani [a], Claudia L. Bianchi [b,c], Muthupandian Ashokkumar [d], Bernaurdshaw Neppolian [a,*]

[a] Department of Chemistry, Faculty of Engineering and Technology, SRM Institute of Science and Technology, Kattankulathur, Chennai 603203, India
[b] Department of Chemistry, University of Milan, Via Golgi 19, 20133 Milano, Italy
[c] Consorzio Interuniversitario Nazionale per la Scienza e Tecnologia dei Materiali (INSTM), via Giusti 9, 50121 Florence, Italy
[d] Sonochemistry Group, School of Chemistry, The University of Melbourne, Parkville, Victoria 3010, Australia

ARTICLE INFO

Keywords:
Copper-BTC
Zinc tungstate
S-scheme heterojunction
Sonophotocatalytic degradation
Tetracycline antibiotic

ABSTRACT

Metal-organic frameworks (MOFs) are a significant class of porous, crystalline materials composed of metal ions (clusters) and organic ligands. The potential use of copper MOF (Cu-BTC) for the sonophotocatalytic degradation of Tetracycline (TC) antibiotic was investigated in this study. To enhance its catalytic efficiency, S-scheme heterojunction was created by combining Cu-BTC with Zinc tungstate ($ZnWO_4$), employing an ultrasound-assisted hydrothermal method. The results demonstrated that the Cu-BTC/$ZnWO_4$ heterojunction exhibited complete removal of TC within 60 min under simultaneous irradiation of visible light and ultrasound. Interestingly, the sonophotocatalytic degradation of TC using the Cu-BTC/$ZnWO_4$ heterojunction showed superior efficiency (with a synergy index of ~0.70) compared to individual sonocatalytic and photocatalytic degradation processes using the same heterojunction. This enhancement in sonophotocatalytic activity can be attributed to the formation of an S-scheme heterojunction between Cu-BTC and $ZnWO_4$. Within this heterojunction, electrons migrated from Cu-BTC to $ZnWO_4$, facilitated by the interface between the two materials. Under visible light irradiation, the built-in electric field, band edge bending, and coulomb interaction synergistically inhibited the recombination of electron-hole pairs. Consequently, the accumulated electrons in Cu-BTC and holes in $ZnWO_4$ actively participated in the redox reactions, generating free radicals that effectively attacked the TC molecules. This study offers valuable perspectives on the application of a newly developed S-scheme heterojunction photocatalyst, demonstrating its effectiveness in efficiently eliminating diverse recalcitrant pollutants via sonophotocatalytic degradation.

1. Introduction

The global use of pharmaceutical drugs has increased due to various factors, such as advanced medical treatments, affordability, and population growth [1]. This has led to the presence of approximately 4,000 active pharmaceutical ingredients in the environment, including wastewater, soil, and drinking water [2]. While the impact of pharmaceuticals on the environment may not always be harmful, concerns have been raised regarding their potential contribution to antimicrobial resistance and long-term effects on biodiversity, such as endocrine disruption in fish [3]. One class of antibiotics that is commonly found in medical and agricultural wastewater as pollutants is tetracycline (TC) antibiotics. These antibiotics are broad-spectrum, inexpensive, and have few side effects, making them a popular choice for treating various bacterial infections such as acne, cholera, and malaria [4]. However, the overuse of tetracycline can lead to the emergence of drug-resistant microorganisms, or superbugs [5]. Additionally, tetracycline discharged into the environment can cause pollution, as it is difficult to degrade naturally due to its stable molecular structure. Residual tetracycline can introduce antibiotic-resistant bacteria and genes into the ecosystem, highlighting the urgent need to regulate its concentration in the environment [6].

* Corresponding author.
E-mail address: neppolib@srmist.edu.in (B. Neppolian).

https://doi.org/10.1016/j.ultsonch.2023.106624
Received 31 July 2023; Received in revised form 27 September 2023; Accepted 27 September 2023

In recent years, Metal organic framework (MOF) material has emerged as a promising material for various research fields, thanks to its unique properties such as high porosity, large specific surface area, and open metal sites [7]. MOFs have been widely used in research areas such as heterogeneous catalysis [8], gas storage and separation, degradation of organic dyes [9], and sensors [10,11]. The 3D pore structure of MOFs provides more active sites for photocatalytic reactions by fixing nanostructured photocatalysts. For instance, Hu et al. (2023) developed a SNP-TiO_2@Cu-MOF photocatalyst that effectively degraded algae (*Karenia mikimotoi*) with a decolorization efficiency of 93.75 % in 6 h [7]. Similarly, Kaur et al. (2021) prepared Cu-TiO_2 nanocomposites derived from Cu-BTC MOF, which showed a degradation rate of 72 % for ofloxacin OFX under visible light for 3 h [12]. Cu-BTC has been shown to be highly stable and possess a high surface area and a band gap of about 3.68 eV, making it a promising material for photocatalytic applications such as the removal of gaseous toluene and the oxidation of thiophenic S-compounds [13,14]. Studies have explored the potential of using Cu-BTC and related materials for the photocatalytic degradation of tetracycline [15,16].

Researchers have shown keen interest in exploring the potential of tungstates as photocatalysts since the discovery of the photocatalytic properties of copper tungstate ($CuWO_4$) in breaking down organic contaminants [17]. While tungstates are typically stable chemically, only a few reports exist on their use as active photocatalysts, with $CdWO_4$, $ZnWO_4$, and Bi_2WO_6 being exceptions. Among them, Zinc tungstate ($ZnWO_4$) has been extensively researched due to its wide bandgap, thermal stability, non-toxicity, and excellent optical and electrical properties [18]. However, its catalytic activity is limited due to the rapid recombination of photo-induced charge carriers, despite its high activity in the UV region. Despite its high activity in the UV region, $ZnWO_4$ has low catalytic activity. Nonetheless, studies have investigated its potential as a photocatalyst for the degradation of tetracycline, with one study demonstrating efficient degradation using 0.10$ZnWO_4$/Bi_2MoO_6 and another using $ZnWO_4$ nanorods as a photocatalyst [19].

Recently, Xu et al. (2020) introduced a novel S-scheme heterojunction comprising of two n-type semiconductors. Their findings revealed that this configuration not only facilitates efficient separation and migration of electron-hole pairs (e^-/h^+), but also effectively maintains their redox ability in the presence of an internal electric field [20]. Subsequently, several studies exploring S-scheme heterojunctions for environmental remediation have emerged [21–31]. Preeyanghaa et al. (2022) synthesized a rod-like g-C_3N_4/V_2O_5 nanocomposite through an ultrasound-assisted thermal polycondensation method, and investigated its application in the sonophotocatalytic degradation of tetracycline [22]. Meanwhile, Zhu et al. (2023) proposed the use of a $Bi_2Sn_2O_7$/β-Bi_2O_3 S-scheme heterojunction photocatalyst for visible-light-driven photocatalytic degradation of tetracycline [32]. Additionally, Wu et al. (2023) demonstrated a highly efficient piezoelectric photocatalyst (V-$BiOIO_3$/FTCN) designed to enhance the removal efficiency of tetracycline [23].

The present study aimed to synthesize a novel S-scheme heterostructure, which combines Cu-BTC and $ZnWO_4$, for enhanced sonophotodegradation efficiency of TC. The heterostructure was designated as Cu-BTC/$ZnWO_4$ heterostructure, and various characterizations and experimental tests were performed to investigate its physicochemical properties and the mechanism behind its improved sonophotodegradation efficiency. Additionally, the effects of key parameters, such as antibiotic and catalyst concentration, solution pH, effect of different water matrices, and scavengers were investigated to determine their impact on the photodecontamination rates of TC. The sonophotocatalytic degradation mechanism of TC and the charge-transfer pathways in the heterostructure were proposed. Furthermore, promising results were obtained for the degradation of TC in real-time analysis of hospital effluent using the same heterostructure.

2. Experimental methods

2.1. Chemicals and instrumentation techniques

Supporting Information (SI) **S1** and **S2** provide detailed information on the chemicals and reagents used, as well as the spectroscopic methods employed to investigate the physicochemical characteristics of the samples.

2.2 . Synthesis of Cu-BTC/$ZnWO_4$ heterostructure

Cu-BTC was synthesized using an ultrasound-assisted hydrothermal method with minor modifications, as described by [33]. The process involved creating Solution A by dissolving benzene-1,3,5-tricarboxylic acid (4.91 g, 23.4 mmol) in ethanol, and Solution B was formed by combining DMF (1:1) (25 mL), $Cu(NO_3)_2{\cdot}3H_2O$ (10.86 g, 46.6 mmol), and deionized water (25 mL) in specific proportions. The solutions were thoroughly mixed on a magnetic stirrer and then subjected to probe sonication (20 kHz; 500 W) before being transferred into an autoclave for hydrothermal treatment at 120 °C for 24 h. Afterward, the resulting mother liquor was decanted, and the product was washed with DMF and ethanol. The isolated solid was subsequently heat-treated under vacuum at 70 °C for 8 h, yielding deep purple Cu-BTC crystals. The synthesized heterostructure was referred to as Cu-BTC.

$ZnWO_4$ was synthesized using a hydrothermal method, with $ZnCl_2{\cdot}6H_2O$ (4 mmol) and $Na_2WO_4{\cdot}2H_2O$ (4 mmol) placed into a 25 mL autoclave vessel with 20 mL of deionized water, and heated to 180 °C for 24 h [34]. To fabricate the Cu-BTC/$ZnWO_4$ heterostructure, the appropriate amount of as-prepared Cu-BTC and $ZnWO_4$ were mixed together with a small quantity of ethanol at a 3:1 M ratio, and the resulting slurry was calcinated at 450 °C for 3 h.

2.3. Sonophotocatalytic degradation experiments

The prepared heterostructure were tested under visible light irradiation (source: 500 W halogen lamp) and ultrasonic irradiator (40 kHz and 600 W) using TC as a model contaminant. About 40 mL of 20 ppm TC solution was used for each experiment with 20 mg photocatalyst. With the aid of a water-circulating cooling device, the temperature of the reaction system was maintained at 25 ± 5 °C. The mixture was stirred for 60 min to attain adsorption–desorption equilibrium. The catalyst was removed by filtering 3 mL of suspension at specific time intervals. To monitor the variations in TC concentration, UV–vis absorption was measured. The recycling experiment was performed for six consecutive cycles. The collected powder after the stability test was characterized using XRD and FTIR to evaluate the stability of the synthesized material. The degradation efficiency (η) was determined by the **Eq. (1)** below:

$$\eta = \left(\frac{C_0\text{-}C}{C_0}\right) \times 100 \quad (1)$$

C_0 and C stand for the initial and residual TC concentration at time 0 and t, respectively. Each sonophotocatalytic experiment was carried out in triplicates at room temperature. The measurement of TOC (Total organic carbon) variations was performed using the Shimadzu TOC-L analyzer. To assess the catalyst's durability, a series of reaction cycles were conducted. To prepare for subsequent rounds of sonophotocatalytic degradation experiments, each catalyst was separated by centrifugation and purified with distilled water. Trapping agents such as 1 mM of IPA (isopropyl alcohol) for •OH (hydroxyl radicals), EDTA (ethylenediaminetetraacetic acid) for h^+ (holes), and BQ (benzoquinone) for $\bullet O_2-$ (superoxide radicals) were employed to examine the reactive species involved in the sonophotocatalytic degradation of TC. This allowed for an investigation into the behavior and presence of these reactive species during the degradation process. Each

sonophotocatalytic experiments were performed in duplicate, and the results demonstrated high repeatability, with less than 5 % relative standard deviation.

3. Results and discussion

3.1. Phase structure, chemical composition, and morphology

The crystalline structure of the synthesized material was investigated using X-ray diffraction (XRD) analysis. The XRD pattern displayed well-defined peaks at specific angles, including 6.85° (200), 9.62° (220), 11.7° (222), 13.52° (400), 14.7° (331), 15.19° (420), 16.60° (422), 17.58° (500), 19.18° (440), 20.35° (600), 21.46° (620), 23.4° (444), 24.21° (551), 25.3° (660), 26.11° (731), 28.82° (822), 29.44° (751), 35.32° (773), and 39.22° (882). These peaks correspond to the characteristic reflections of pure Cu-BTC (Fig. 1a), exhibiting a face-centred cubic (FCC) crystal structure and align with the previous studies [35–37], providing further evidence of the purity and structural integrity of Cu-BTC. Similarly, the XRD pattern of pristine $ZnWO_4$ showed distinct peaks localized around 2θ values of 15.5° (010), 18.9° (100), 23.8° (011), 24.6° (110), 30.6° (−111), 31.3° (020), 36.4° (021), 38.4° (200), 41.3° (210), 44.3° (−112), 45.5° (−211), 47.7° (030), 48.8° (022), 50.3° (220), 51.8° (130), 52.6° (122), 53.7° (202), 55.3° (−131), 56.3° (−212), 58.5° (300), 61.8° (−113), 62.8° (230), 63.4° (−222), 64.0° (−311), 64.8° (−132), 65.5° (040), 68.3° (041), and 71.7° (−141), according to JCPDS card #73–0554 (Fig. 1a) [38], exhibiting a monoclinic crystal structure [39]. The prominent peaks at (222) and (−111) indicate the preferential orientation of the synthesized Cu-BTC and $ZnWO_4$, respectively. The XRD pattern of Cu-BTC/$ZnWO_4$ heterostructure exhibited distinct diffraction peaks corresponding to Cu-BTC and $ZnWO_4$, confirming their presence in the synthesized hybrid heterostructure.

Fourier Transform Infrared Spectroscopy (FTIR) was employed to investigate the chemical structure and internal molecular bonding of the Cu-BTC/$ZnWO_4$ in the range of 4000–400 cm^{-1} (Fig. 1b). The spectra of the Cu-BTC/$ZnWO_4$ heterostructure exhibited characteristic peaks of Cu-BTC and $ZnWO_4$. These findings confirm the successful synthesis of the Cu-BTC/$ZnWO_4$ heterostructure, in accordance with XRD and FESEM observations. Broad peaks observed from 3600 to 3000 cm^{-1} were attributed to the bending and stretching vibrations of surface-adsorbed water molecules, resulting from moisture in the air and the hydrothermal treatment of the samples [40]. In the FTIR spectrum of Cu-BTC, several characteristic peaks were observed. The presence of strong peaks around 1362 cm^{-1} indicated the asymmetric and symmetrical stretching vibrations of the carboxylate groups, implying their active involvement in coordination with copper(II) ions and the formation of metal–organic frameworks [41]. Peaks in the range of 1500–1600 cm^{-1} were associated with vibrations of the benzene ring, confirming the presence of the aromatic moiety in the Cu-BTC structure. Metal-ligand interactions were evident from peaks in the range of 400–900 cm^{-1}, signifying the presence of metal–ligand vibrations and demonstrating the coordination of copper (II) ions with the carboxylate groups. These peaks provided evidence of the formation of coordination bonds between the metal center and the ligand in Cu-BTC. The strong peaks of $ZnWO_4$ were observed at 806 cm^{-1} indicated the stretching vibrations of the tungstate groups, confirming the presence of tungstate anions and their significant role in the molecular structure of $ZnWO_4$. Peaks in the range of 400–700 cm^{-1} were attributed to metal–oxygen vibrations, specifically the zinc-oxygen bonds in $ZnWO_4$, providing information about the metal–oxygen coordination in the compound. In the FTIR spectrum of the Cu-BTC/$ZnWO_4$ heterostructure, overlapping or closely positioned characteristic peaks of both Cu-BTC and $ZnWO_4$ were expected. This confirmed the successful incorporation of both materials within the heterostructure material.

XPS analysis was conducted to investigate the chemical states and bonding configuration of the synthesized samples (Fig. 2). Fig. 2a displays the survey spectra of Cu-BTC, $ZnWO_4$, and the Cu-BTC/$ZnWO_4$ heterostructure, revealing signals corresponding to Cu, C, Zn, W, and O elements without any detected impurities. The high-resolution Cu 2p spectrum (Fig. 2b) displays five peaks at 962.82, 954.04, 944.96, 941.80, and 934.09 eV, where the peaks at 934.09 and 954.04 eV are assigned to Cu $2p_{3/2}$ and Cu $2p_{1/2}$ of Cu–O, respectively. The presence of overlapping satellite peaks at 943.96 and 941.80 eV for Cu $2p_{3/2}$ and at 962.82 eV for Cu $2p_{1/2}$ suggests the presence of CuO (Cu^{2+}) or Cu_2O (Cu^{1+}) species in the heterostructure [42]. The C 1 s XPS spectrum in Fig. 2c reveals three peaks at 284.71, 286.80, and 288.80 eV, corresponding to C–C & C–H & C = C, C–O, and O–C–O groups, respectively. The binding energies of Zn $2p_{1/2}$ and Zn $2p_{3/2}$ peaks located at ~1044.04 and ~1020.91 eV in $ZnWO_4$ [43] are shown in Fig. 2d. The two bands located at 37.35 and 39.55 eV are ascribed to W $4f_{7/2}$ and W $4f_{5/2}$, respectively (Fig. 2e). In Fig. 2f, a prominent peak at 529.91 eV can be attributed to the distinct bands associated with the oxygen atoms in $ZnWO_4$. The crystalline structure reveals an oxygen anion at a binding energy of 531.45 eV, indicating the presence of an oxygen vacancy region, as observed in the XPS signal of O 1 s. Additionally, a smaller peak at 532.65 eV can be attributed to surface-bound water or adsorbed oxygen. Collectively, these results provide convincing evidence of the successful fabrication of the Cu-BTC/$ZnWO_4$ heterostructure.

The structural morphology of the samples was analyzed using Field emission scanning electron microscopy (FE-SEM) (Fig. 3a-c) and high-

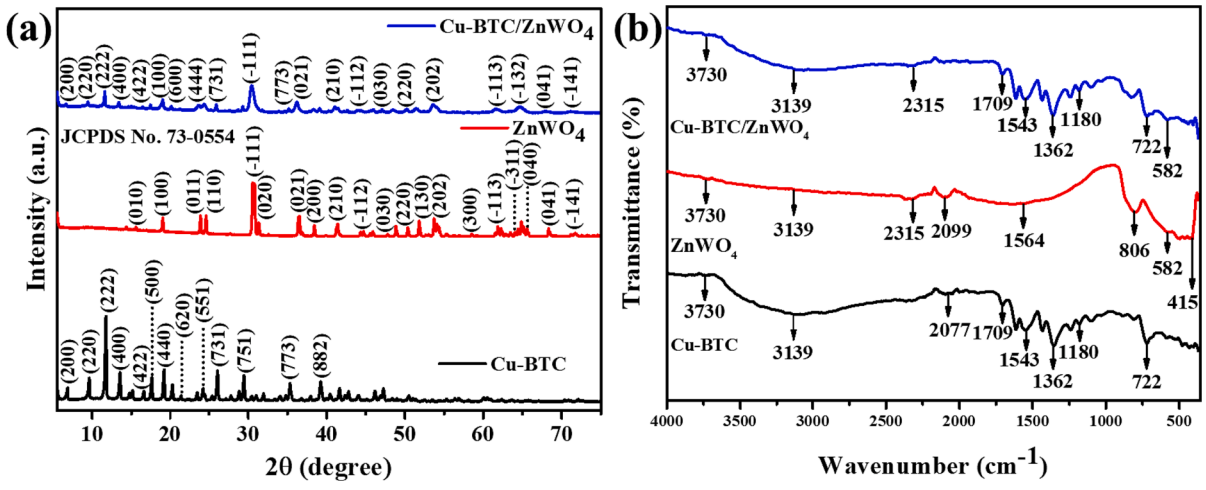

Fig. 1. (a) XRD patterns and (b) FTIR spectra of Cu-BTC, $ZnWO_4$ and Cu-BTC/$ZnWO_4$ heterostructure.

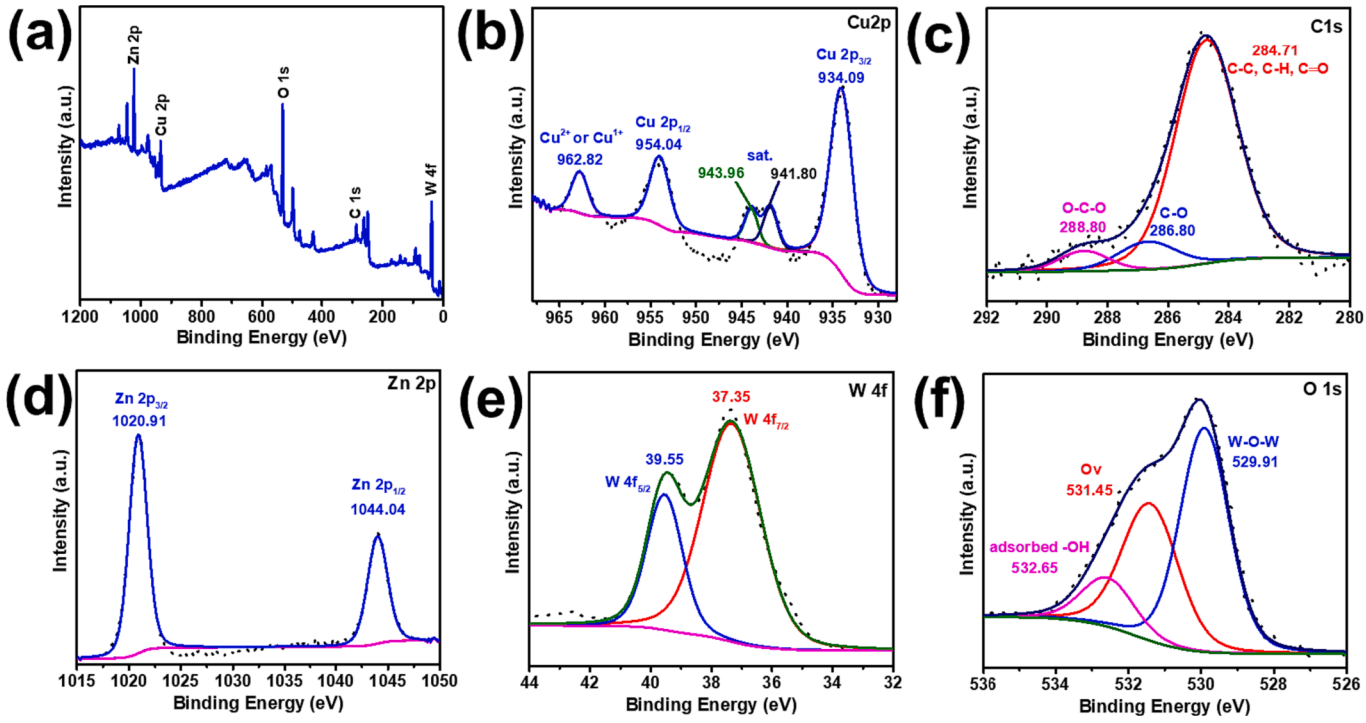

Fig. 2. (a) XPS survey spectra of Cu-BTC, $ZnWO_4$ and Cu-BTC/$ZnWO_4$ heterostructure. High-resolution XPS spectra: (b) Cu 2p, (c) C 1 s, (d) Zn 2p, (e) W 4f, (f) O 1 s of Cu-BTC, $ZnWO_4$ and Cu-BTC/$ZnWO_4$ heterostructure.

resolution transmission electron microscopy (HR-TEM) (Fig. 3d-f). The FE-SEM spectrum in Fig. 3a reveals flower-like structures of Cu-BTC nanoparticles. Additionally, Fig. 3b shows that $ZnWO_4$ exhibited irregular-shaped particles. As depicted in Fig. 3c and f, it is evident that Cu-BTC nanoparticles are well dispersed and decorated with $ZnWO_4$ nanoparticles, indicating the formation of the Cu-BTC/$ZnWO_4$ heterostructure. To gain further insight into the crystal structure of the Cu-BTC/$ZnWO_4$ heterostructure, HR-TEM analysis was conducted. Fig. 3d shows the random decoration of Cu-BTC nanoparticles on the surface of $ZnWO_4$. The lattice fringes observed in the HR-TEM image confirm the high crystallinity of Cu-BTC/$ZnWO_4$ heterostructure. The measured interplanar spacing (d) in the HR-TEM image is approximately 2.92 Å, corresponding to the (−1 1 1) plane of $ZnWO_4$, consistent with the X-ray diffraction (XRD) results. The lattice spacing (d = 1.9 Å) corresponds to Cu-BTC. The clear and interlaced lattice fringes of Cu-BTC and $ZnWO_4$ on the catalyst demonstrate the formation of heterostructures, facilitating charge transfer between Cu-BTC and $ZnWO_4$ (**Fig. S1**). Additionally, a Fast fourier transform (FFT) pattern taken from the same area confirms the single crystalline nature of the composite (Fig. 3g). The SAED patterns, depicted in Fig. 3h, exhibit concentric patterns indicative of diffraction planes. Specifically, these patterns reveal the presence of the (2 2 2) plane for Cu-BTC and the (2 1 2), (2 0 0), and (−1 1 1) planes for $ZnWO_4$ within the Cu-BTC/$ZnWO_4$ heterostructure. These identified planes align consistently with the d-spacing values derived from the XRD patterns. To confirm the elemental composition of the Cu-BTC/$ZnWO_4$ heterostructure, elemental mapping and EDAX spectrum were performed, as shown in Fig. 3 **(i-m)** and **3n**, respectively. The results indicate the presence of Cu, C, Zn, W and O elements without any impurities inside the Cu-BTC/$ZnWO_4$ heterostructure. Furthermore, Fig. 3 **(i-m)** presents the distribution of these elements, with Cu, C, O, Zn, and W represented by pink, red, and yellow, respectively. This confirms that the XRD and XPS analysis results are in agreement and provide insights into the formation of the Cu-BTC/$ZnWO_4$ heterostructure.

The specific surface area and pore diameter of the synthesized samples were estimated using the BET analysis. **Fig. S2** and **Table S1** present the corresponding plots and pore diameter of the Cu-BTC, $ZnWO_4$, and Cu-BTC/$ZnWO_4$ heterostructure. The results indicate that the nitrogen adsorption–desorption isotherms exhibit type-IV curves, indicating a mesoporous structure. The BET surface areas of Cu-BTC, $ZnWO_4$, and Cu-BTC/$ZnWO_4$ heterostructure were 943, 37, and 1644 m^2/g, respectively, as depicted in **Fig. S2 (a, c, and e)**. This implies that the Cu-BTC/$ZnWO_4$ heterostructure possesses a higher number of surface-active sites compared to the pristine samples. Additionally, the average BJH pore diameter of Cu-BTC, $ZnWO_4$, and Cu-BTC/$ZnWO_4$ heterostructure were determined to be 14, 4, and 3 nm, respectively, as shown in **Fig. S2 (b, d, and f)**. The increased surface area of the Cu-BTC/$ZnWO_4$ heterostructure resulted from the presence of smaller pores, promoting superior sonophotocatalytic activity. This enhancement is attributed to the abundance active sites, which in turn leads to improved adsorption efficiency during the remediation of organic contaminants.

3.2. Optical absorption and photogenerated charge carrier behavior

The optical properties of the photocatalysts were studied using UV–vis DRS and the absorption spectra obtained for Cu-BTC, $ZnWO_4$, and Cu-BTC/$ZnWO_4$ shown in Fig. 4a. Cu-BTC exhibits a strong absorption band in the visible light range at around 457.9 nm, indicating its efficient absorption of visible light. In addition, the absorbance and Kubelka-Munk formula can be used to determine the energy band gap of the developed samples as depicted in **Eq. (2)**.

$$(\alpha h\vartheta)n = k\left(h\vartheta - E_g\right) \tag{2}$$

The absorption coefficient, constant, photon energy, absorption band gap energy, and semiconductor type are represented by α, k, hν, E_g, and n, respectively, in the formula. The relationship between $(\alpha h\nu)^2$ and hν for the sample is illustrated in Fig. 4b. A significant difference in the E_g is expected when comparing Cu-BTC/$ZnWO_4$ (1.25 eV) to pristine Cu-BTC and $ZnWO_4$. This difference in E_g is anticipated to reduce the energy barrier for the e^-/h^+ pair generation, thereby enhancing the sonophotocatalytic efficiency of the heterostructure.

The calculated band gap of Cu-BTC is 2.7 eV, suggesting the presence of indirect band gap characteristics and the involvement of phonons in

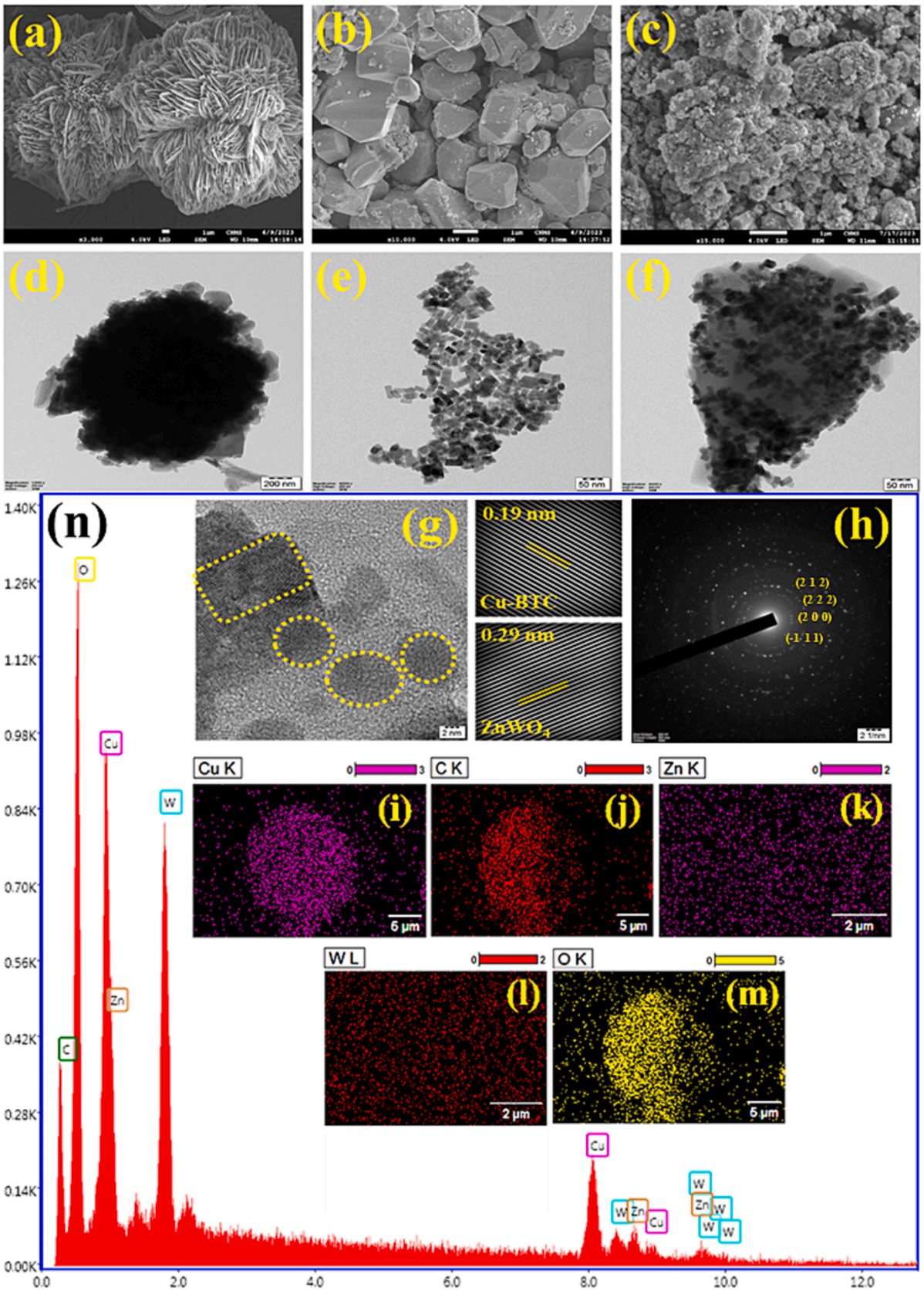

Fig. 3. FE-SEM images of (a) Cu-BTC, (b) $ZnWO_4$, and (c) Cu-BTC/$ZnWO_4$ heterostructure. HR-TEM images of (d) Cu-BTC, (e) $ZnWO_4$, and (f) Cu-BTC/$ZnWO_4$ heterostructure. (g) HR-TEM image of Cu-BTC/$ZnWO_4$ heterostructure with FFT pattern. (h) Selective area electron diffraction of Cu-BTC/$ZnWO_4$ heterostructure. (i-m) Mapping of corresponding elements (Cu, C, O, Zn, and W) of Cu-BTC/$ZnWO_4$ heterostructure. (n) EDAX spectrum of Cu-BTC/$ZnWO_4$ heterostructure.

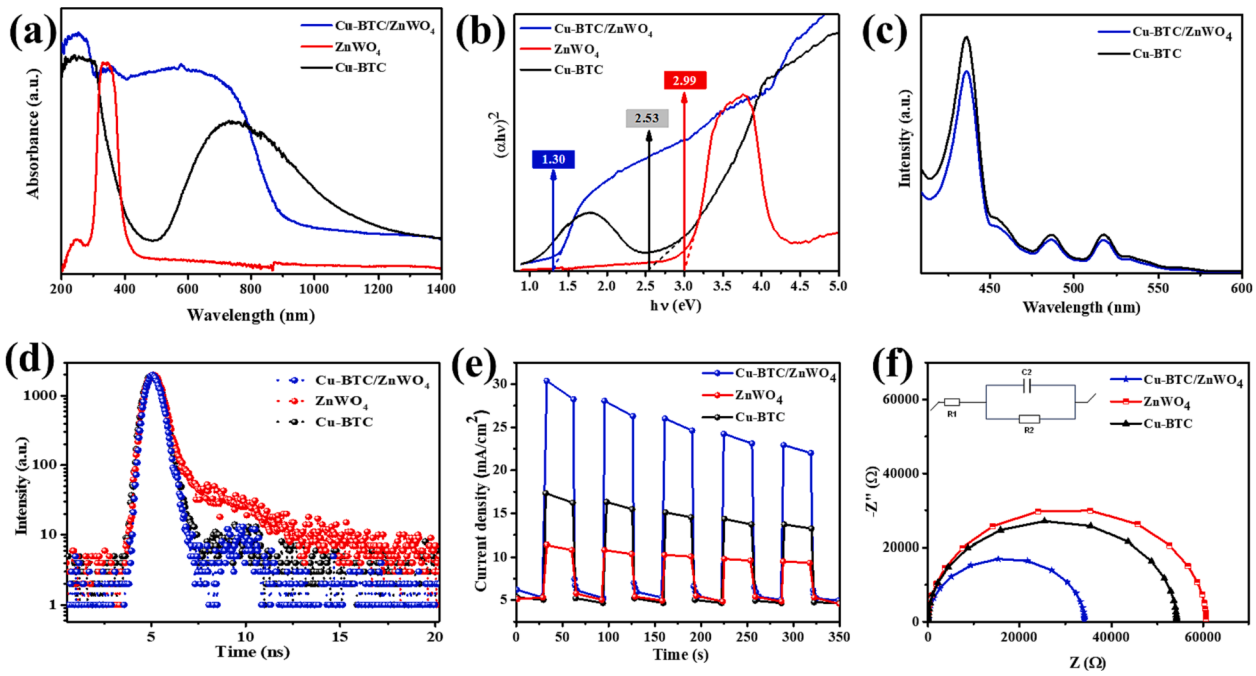

Fig. 4. (a) UV–vis spectra (b) Tauc plots (c) PL spectra (d) TRPL spectra (e) photocurrent response (f) EIS spectra of Cu-BTC, $ZnWO_4$ and Cu-BTC/$ZnWO_4$ heterostructure.

electron transitions [14,44]. Similarly, $ZnWO_4$ displays a prominent absorption peak in the visible light range around 413 nm, indicating its effective absorption of visible light. In line with literature reports [45–47], $ZnWO_4$ with a band gap of 3.0 eV is also known to involve phonons in electron transitions. On the other hand, Cu-BTC/$ZnWO_4$ demonstrates an absorption peak in the near-infrared range at 958.7 nm, indicating its dominant light absorption in the near-infrared region. The band gap of Cu-BTC/$ZnWO_4$ is calculated to be 1.25 eV, confirming its indirect band gap characteristics. These findings highlight the materials' ability to absorb light in different regions of the electromagnetic spectrum and provide valuable insights for their potential applications in optoelectronic devices and energy conversion systems.

Efficient transfer and migration of e^-/h^+ charge carriers play a critical role in the field of sonophotocatalytic applications. As depicted in Fig. 4c, the Cu-BTC has high PL intensity which indicates a high recombination rate of e^-/h^+, which can limit the sonophotocatalytic activity. When e^-/h^+ recombine, the energy that could have been used for catalytic reactions is lost as heat or emitted as light. Therefore, a high PL intensity is generally associated with low sonophotocatalytic activity [48]. Conversely, Cu-BTC/$ZnWO_4$ heterostructure has low PL intensity, demonstrating efficient charge carier separation and reduced recombination, which is desirable for enhanced sonophotocatalytic activity [49]. When e^-/h^+ pairs are effectively separated, they can participate in redox reactions with adsorbed species, leading to the degradation of pollutants or the production of desired products. Therefore, a low PL intensity is often correlated with high sonophotocatalytic activity [50]. Additionally, the incorporation of $ZnWO_4$ promotes e^- migration within the Cu-BTC/$ZnWO_4$ heterostructure, leading to lower recombination efficiency. This suggests that the combination of Cu-BTC and $ZnWO_4$ effectively facilitates the transfer of photo-induced charges, thereby significantly decreasing the rate of radiative recombination (e^-/h^+).

Further evaluation of the recombination dynamics of photo-excitons was conducted through time-resolved photoluminescence (TRPL) decay spectra, as illustrated in Fig. 4d. The average lifetime of the Cu-BTC/$ZnWO_4$ heterostructure (4 ns) was found to be higher than that of Cu-BTC (3.19 ns) and $ZnWO_4$ (1.43 ns).

To gain a deeper understanding of photo-induced charge separation and charge transfer resistance, electrochemical impedance spectroscopy (EIS) and transient photocurrent analysis were performed on Cu-BTC, $ZnWO_4$, and Cu-BTC/$ZnWO_4$ heterostructure. The heterostructure's transient photocurrent responses were measured during multiple light on/off cycles, as depicted in Fig. 4e. Among the samples, the Cu-BTC/$ZnWO_4$ heterostructure demonstrates a higher photocurrent density. This is attributed to its enhanced ability to absorb visible light and its efficient separation of e^-/h^+ pairs, resulting in improved performance [51]. Fig. 4f presents the Nyquist plots of Cu-BTC, $ZnWO_4$, and the Cu-BTC/$ZnWO_4$ heterostructure. By comparing the arc radius of the EIS plots, valuable insights into enhanced e^- transfer can be obtained. A smaller arc radius indicates improved photogenerated charge carrier separation and reduced charge-transfer resistance at the interface. Remarkably, the heterostructure exhibited a significantly reduced arc radius compared to the other samples. This suggests that the Cu-BTC/$ZnWO_4$ heterostructure possesses the lowest charge-transfer resistance and exhibits excellent electro-conductivity, which greatly enhances the separation and migration of photo-generated e^-/h^+ pairs. Thus, the Cu-BTC/$ZnWO_4$ heterostructure demonstrates superior recombination efficiency, higher lifetime, and improved charge-transfer resistance, exhibiting enhanced sonophotocatalytic properties and efficient transfer of photo-induced charges. In order to confirm the band edge potential and semiconductor characteristics of Cu-BTC and $ZnWO_4$, Mott-Schottky (MS) plots were employed to investigate their electronic band structures. The MS plots for Cu-BTC and $ZnWO_4$ are illustrated in **Fig. S3**a and S3b. Both materials exhibited the characteristics of n-type semiconductors, and their respective flat-band potentials were measured at 2.67 and 3.07 V (vs. Ag/AgCl), respectively.

3.3. Sonophotocatalytic degradation of TC

The sonophotocatalytic performance of Cu-BTC, $ZnWO_4$, and Cu-BTC/$ZnWO_4$ was assessed by studying the degradation of TC antibiotics under simultaneous exposure to ultrasound and simulated light. Fig. 5 presents the results of the degradation efficiency of the synthesized catalysts in terms of change in TC concentration (C/C_0), where C represents the TC concentration after catalytic activity and C_0 represents the initial TC concentration. TC cannot be effectively degraded solely by sonolysis (9 %), photolysis (24 %), and sonophotolysis (27 %) (**Fig. S4 a-**

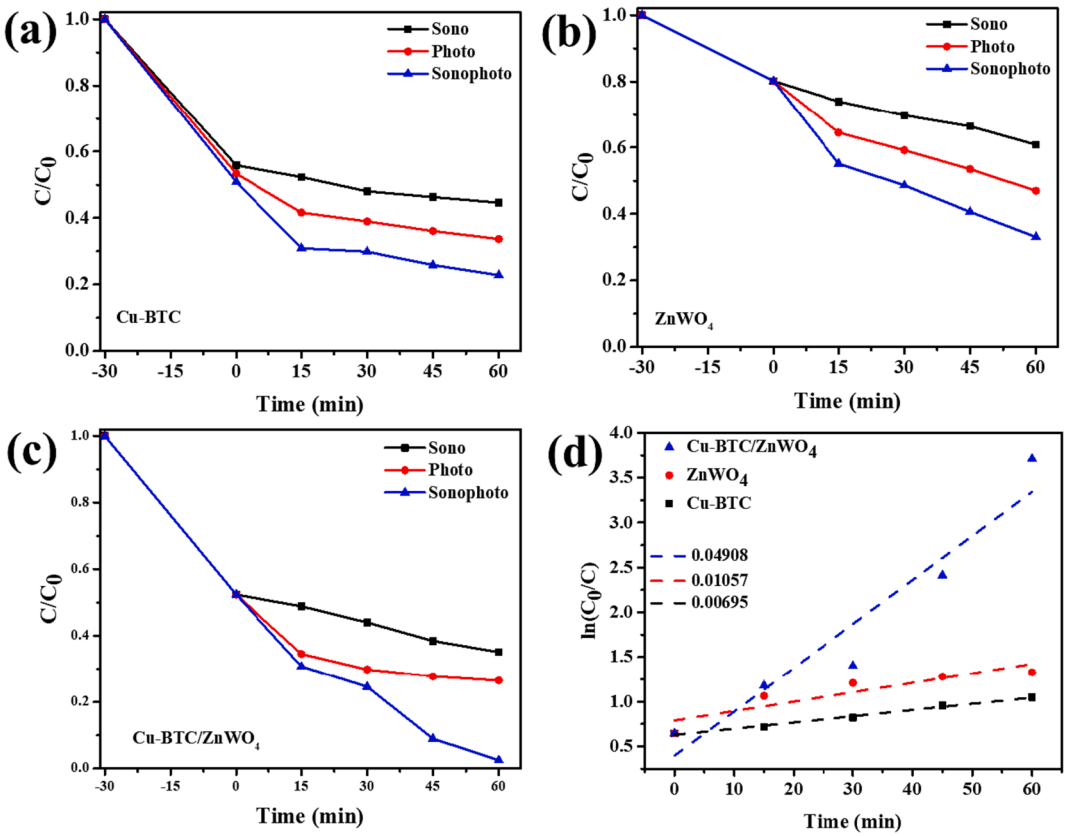

Fig. 5. The degradation of TC over (a) Cu-BTC, (b) $ZnWO_4$, and (c) Cu-BTC/$ZnWO_4$ was analyzed using C/C_0 plots for sono-, photo-, and sonophotocatalytic processes (d) Kinetic study of Cu-BTC, $ZnWO_4$, and Cu-BTC/$ZnWO_4$.

c) due to the significant loss of reactive oxygen species (ROS) before they can attack TC [52]. However, when ultrasound and/or light irradiation were applied in combination with catalysts for 60 min, the degradation of TC using the synthesized catalysts was significantly enhanced due to the involvement of various reactive species. Fig. 5a, b, and c demonstrate the effectiveness of sonocatalysis in degrading TC, with degradation efficiencies of 55 % for Cu-BTC, 39 % for $ZnWO_4$, and 64 % for Cu-BTC/$ZnWO_4$, respectively. In sonocatalytic systems, hydroxyl radicals (•OH) play a major role in the degradation of antibiotics. The high degradation effectiveness observed under sonication can be attributed to the catalysts' ability to generate ROS and subsequent radical reactions [53]. Hydrogen peroxide (H_2O_2) and •OH species produced during the process react with TC, further enhancing the sonocatalytic performance under the given conditions [24]. Additionally, the acoustic cavitation effect of ultrasound is believed to contribute to the improved TC degradation efficiency by increasing the catalyst's surface area and active sites through mass transfer and generating a large number of free radicals via sonoluminescence [54].

However, despite 60 min of ultrasonic irradiation with catalysts, complete degradation of TC could not be achieved, possibly due to the loss of dissolved gases [55], formation of intermediates [56], and specific reaction conditions [57]. On the other hand, the degradation efficiency of TC under photocatalysis was found to be 66 % for Cu-BTC, 50 % for $ZnWO_4$, and 74 % for Cu-BTC/$ZnWO_4$, employing the conventional mechanism of e^-/h^+ pairs. Photocatalysis exhibited higher TC degradation efficiency compared to sonocatalysis, primarily because of direct exposure to higher photon energy rather than the secondary impact of ultrasound [58]. However, the complete degradation of TC through photocatalysis was limited by constraints such as mass transfer and light penetration.

In the case of simultaneous ultrasound and light irradiation, the TC degradation efficiency increased to 65 % for Cu-BTC, 74 % for $ZnWO_4$, and 98 % for Cu-BTC/$ZnWO_4$, as shown in Fig. 5a, b, and c**.** The absorption spectra of sonophotocatalysis are depicted in **Fig. S4**d. Consequently, the Cu-BTC/$ZnWO_4$ catalysts demonstrated superior TC degradation efficiency compared to Cu-BTC and $ZnWO_4$ individually. The sonophotocatalytic performance of Cu-BTC, $ZnWO_4$ and Cu-BTC/$ZnWO_4$ are evaluated by the degradation of TC antibiotics under simultaneous irradiation of ultrasound and simulated light. The degradation efficiency of TC using Cu-BTC and $ZnWO_4$ catalysts shows the following trend: sonocatalysis < photocatalysis < sonophotocatalysis. This suggests that the combined effect of sonophotocatalysis exhibits superior performance compared to the individual processes of sonocatalysis and photocatalysis alone. To quantify the synergistic effect, **Eqs. (3) and (4)** were employed. The results indicate that the Cu-BTC/$ZnWO_4$ heterostructure achieves complete degradation of TC, with a synergy index of 0.70 during sonophotocatalytic degradation. Furthermore, a kinetic investigation of TC sonophotocatalytic degradation was carried out under ideal experimental conditions to quantitatively assess mineralization efficiency. The rate constant (k) was determined from the slope of the linear plot Fig. 5d using the linear connection of the Langmuir-Hinshelwood model $\ln(C_0/C)$ versus time (min) represented in **Eq. (5)**.

$$\text{Synergy index} = \frac{[\text{Sonophotocatalytic TC degradation efficiency } (\%)]}{[\text{Sonocatalytic TC degradation efficiency } (\%)] + [\text{Photocatalytic TC degradation efficiency}(\%)]} \quad (3)$$

$$\text{Synergy index} = \frac{\text{K[Sonophoto. Cu-BTC/ZnWO}_4\text{]}}{\text{[K(Sono.Cu-BTC/ZnWO}_4\text{)]} + \text{[K(Photo. Cu-BTC/ZnWO}_4\text{]}} \quad (4)$$

$$ln\frac{C_0}{C} = kt \quad (5)$$

where C_0 and C denote the initial and final TC concentrations at time 0 and t (min), respectively, and k is the rate constant. The correlation coefficient value ($R^2 > 0.90$) of the as-developed catalyst indicates that the experimental data were suitably compatible with the pseudo-first-order kinetic model. The estimated rate constant values of Cu-BTC, $ZnWO_4$, and Cu-BTC/$ZnWO_4$ heterstructure were determined to be (k – 0.00695 min^{-1}), (k – 0.01057 min^{-1}), and (0.04908 min^{-1}). The obtained results highlight that Cu-BTC/$ZnWO_4$ heterostructure has superior sonophotocatalytic degradation rate, which was 7 and 4 times faster than the pure Cu-BTC and $ZnWO_4$, respectively. Moreover, Table 1 presents a compilation of various catalysts used in sonophotocatalytic degradation experiments to eliminate pharmaceutical compounds. The catalysts include $Ag_6Si_2O_7/SmFeO_3$, MoS_2/C, g-C_3N_4, $CoFe_2O_4$@-TiO_2@rGO, SnO_2, Ca-doped ZnO, Ni – Ti LDH@g-C_3N_4, CdS/ZnO, NiFe-LDH/rGO heterostructure, $Bi_2MoO_6/FeVO_4$, $CuFe_2O_4$/montmorillonite, Ti^{3+}-self-doped TiO_2, PM-TiO_2-Pd, CQD-B-ECN, rGO/Ag_2CO_3. The sonophotocatalytic degradation efficiencies for different pharmaceutical compounds (e.g., Ciprofloxacin, Levofloxacin, Tetracycline, Amoxicillin, Moxifloxacin) range from 79.44 % to 100 %. The catalysts, along with specific light sources and sonication methods, influence the degradation efficiency. Notably, the sonophotocatalytic performance of Cu-MOF/$ZnWO_4$ surpasses that of most catalysts mentioned. It achieved a degradation efficiency of 98 % within 60 min, making it the best catalyst among those studied. This indicates that Cu-MOF/$ZnWO_4$ holds significant potential as an effective catalyst for the degradation of TC compound through sonophotocatalysis.

The pH of the working solution plays a crucial role in determining the efficiency of degradation. It is a significant factor as it influences the surface charge and size of the aggregates that are formed. To assess the impact of pH, the experiments are conducted within a range of 2.0 to 12.0, under optimized conditions (Cu-BTC/$ZnWO_4$ dosage – 0.2 g/L, TC concentration – 20 mg/L) (Fig. S5a). The results showed that the mineralization efficiency of TC increased from 48 % to 98 % as the pH increased from 2.0 to 7.0. This finding was consistent with the study by He et al. (2022) [73]. However, when the pH was further increased from 7.0 to 12.0, the efficiency (η) decreased to 35 %. This can be attributed due to the formation of by-products or intermediates that hinder the degradation of the target compound.

The impact of Cu-BTC/$ZnWO_4$ dosage on TC mineralization was investigated by varying the catalyst amount (0.1–0.5 g/L) while keeping the TC concentration constant at 20 mg/L. Multiple sonophotocatalytic degradation runs were conducted, and the results were analyzed (Fig. S5b). The findings revealed that the initial degradation rates were directly proportional to the catalyst dosage within the range of 0.1–0.3 g/L, and this positively influenced the mineralization efficiency. Increasing the Cu-BTC/$ZnWO_4$ dosage from 0.1 to 0.3 g/L resulted in a significant enhancement of the η value, with an increase from 73 % to 98 %. The enhanced sonophotocatalytic performance is attributed to the effective absorption of light by more reactive sites when the catalyst dosage is increased [74]. However, in this specific reaction at 40 kHz, further increasing the catalyst amount leads to a reduction in the degradation efficiency by up to 84 %. This can be explained by the following factors: (i) Suppressed energy transfer occurs due to the blocking of ultrasonic radiation; (ii) the presence of solution turbidity

Table 1
Evaluation of various photocatalyst performance for the sonophotocatalytic degradation of pharmaceutical compounds.

Catalysts	Pollutants	Source	Sonophoto-catalytic degradation (%)	Duration time (min)	Ref.
$Ag_6Si_2O_7/SmFeO_3$ (0.6 g/L)	Ciprofloxacin (10 mg/L)	LED lamp (250 W); Bath sonicator (40 kHz)	94.9	60	[52]
MoS_2/C (0.01 g/L)	Levofloxacin (70 mg/L)	Xenon lamp (300 W); Horn-type sonicator (40 kHz)	100	180	[59]
g-C_3N_4 (0.01 g/L)	Tetracycline (15 mg/L)	Halogen lamp (300 W); Bath sonicator (40 kHz)	96	60	[60]
$CoFe_2O_4$@TiO_2@rGO (0.03 g/L)	Tetracycline (20 mg/L) and Ciprofloxacin (10 mg/L)	Halogen lamp (500 W); Bath sonicator (40 kHz)	92 – TC84 -Ciprofloxacin	90	[61]
SnO_2 (3 g/L)	Tetracycline (20 mg/L)	LED light (9 W); Bath sonicator (40 kHz)	88.82	135	[62]
Ca-doped ZnO (25 mg/50 mL)	Tetracycline (10 mg/L)	White LED strip (1.6 W); Bath sonicator (40 kHz)	100	90	[63]
Ni – Ti LDH@g-C_3N_4 (1.25 g/L)	Amoxicillin (1.0 g/L)	Mercury lamp (500 W); Horn-type sonicator (20 kHz)	99.5	75	[64]
CdS/ZnO (0.4 M ratio)	Tetracycline (30 mg/L)	Xenon lamp (100 W); Bath sonicator (50 kHz)	84	90	[65]
NiFe-LDH/rGO heterostructure (1.0 g/L)	Moxifloxacin (20 mg/L)	LED lamp (10 W); Bath-type sonicator (36 kHz)	90.40	60	[66]
$Bi_2MoO_6/FeVO_4$ (0.5 g/L)	Ciprofloxacin (20 mg/L)	Xenon lamp (500 W); Bath sonicator (40 kHz)	98.20	60	[67]
$CuFe_2O_4$/montmorillonite (0.6 g/L)	Ciprofloxacin (50 mg/L)	UV mercury lamp; Bath sonicator (50 kHz)	93.1	60	[68]
Ti^{3+}-self-doped TiO_2 (0.04 g/L)	Tetracycline (9 mg/L)	Halogen lamp (300 W); Bath sonicator (40 kHz)	84	60	[69]
PM-TiO_2-Pd (0.5 g/L)	Ciprofloxacin (20 mg/L)	LED (10 W); Bath sonicator (40 kHz)	79.44	120	[70]
CQD-B-ECN (0.04 g/L)	Tetracycline (15 mg/L)	Halogen lamp (300 W); Bath-type sonicator (40 kHz)	100	180	[71]
rGO/Ag_2CO_3 (0.3 g/L)	Tetracycline (10 mg/L)	Xenon lamp (500 W); Horn-type sonicator (33 kHz)	97.3	60	[72]
Cu-MOF/$ZnWO_4$ (0.02 g)	Tetracycline (20 mg/L)	Halogen lamp (500 W); Bath-type sonicator (40 kHz)	98	60	**Present study**

affects light penetration; and (iii) self-consumption of ROS happens at the liquid–gas interface. Based on these findings, an optimal catalytic dosage of 0.2 g/L was selected for further studies.

The impact of TC concentration on the mineralization efficiency of Cu-BTC/$ZnWO_4$ was investigated by varying the TC concentration in the range of 10 to 30 mg/L, while keeping the Cu-BTC/$ZnWO_4$ dosage constant at 0.2 g/L (**Fig. S5**c). Multiple photodecomposition runs were conducted to analyze the effect. The experimental results demonstrate that a TC concentration of 20 mg/L achieved nearly complete degradation of TC (~98 %). However, as the TC concentration increased, the sonophotocatalytic efficiency (η) decreased [75]. This decline in η can be attributed to a limited production of oxidative species, as the active sites on the catalyst surface become occupied by TC molecules and intermediate by-products of TC degradation. Additionally, higher TC concentrations increase the likelihood of competition between TC and Cu-BTC/$ZnWO_4$ for the absorption of incident photons.

3.4. Sonophotocatalytic mechanism and degradation pathways of TC

To examine how free radicals are generated and transferred during the reaction, Electron Spin Resonance (ESR) analysis was utilized to investigate the presence of OH•, h^+, and $O_2•^-$ under light exposure [76,77]. The ESR spectra of OH•, and $O_2•^-$ observed for Cu-BTC/$ZnWO_4$ heterostructure is illustrated in Fig. 6a, and b. In the absence of light, no signals for OH• or $O_2•^-$ were detected. However, upon light irradiation, the intensity of OH• in the Cu-BTC/$ZnWO_4$ heterostructure exhibited a significant increase (Fig. 6a). Similarly, the production of $O_2•^-$ in Cu-BTC/$ZnWO_4$ heterostructure was notably higher, indicating enhanced $O_2•^-$ generation after the formation of the heterostructure (Fig. 6b). To investigate the ROS generated during the degradation of TC by Cu-BTC/$ZnWO_4$ heterostructure, trapping studies were conducted utilizing scavengers such as BQ, IPA, and EDTA. Fig. 6d illustrates the outcomes of these studies. The efficiency of sonophotocatalytic TC degradation was significantly reduced in the presence of BQ, decreasing from 98 % to 39 %. Similarly, the presence of IPA resulted in a degradation efficiency of approximately 44 %. EDTA, when employed as a scavenger, caused a drop of about 84 % in the TC degradation efficiency. These findings indicate that h^+, as reactive species, play a dominant role in the degradation of TC. These findings provide strong evidence that the coupling of Cu-BTC and $ZnWO_4$ promotes the generation of OH•, and $O_2•^-$.

Based on the preceding discussion, a plausible mechanism for the charge transfer during the sonophotocatalytic degradation of TC has been proposed and illustrated in Fig. 7. In line with the equation ($E_{CB} = E_{VB} - E_g$), the calculated values of CB edges for Cu-BTC and $ZnWO_4$ were determined as + 0.14 and + 0.08 V (vs Ag/AgCl), respectively. When subjected to ultrasonic irradiation and visible light, both Cu-BTC and $ZnWO_4$ generated e^-/h^+ pairs at their surfaces, which rapidly separated. The h^+ on the VB of Cu-BTC exhibited strong oxidation capability towards OH– ions, resulting in the formation of •OH radicals. Due to the redox potential of $O_2/•O_2^-$ (0.33 eV vs. NHE), the CB potentials of both Cu-BTC and $ZnWO_4$ were unable to generate $•O_2^-$ radicals, consistent with the findings from ESR analysis. Moreover, the accumulated e^- on the CB of $ZnWO_4$ reacted with O_2 to produce H_2O_2 through multiple electron reduction. The work functions (Φ) of n-type Cu-BTC and n-type $ZnWO_4$ were determined as 5.5 and 5.13 eV, respectively [78], as shown in Fig. 6c. By analyzing the differences in Fermi level (E_F), using the equation $\Phi = E_0 - E_F$, where E_0 represents the static electron energy in the vacuum on the material surface, it was observed that when Cu-BTC and $ZnWO_4$ were combined without irradiation, the e^- migrated from Cu-BTC to $ZnWO_4$ due to the higher E_F of Cu-BTC compared to $ZnWO_4$. This migration continued until the E_F reached equilibrium, resulting in band edge bending (Cu-BTC upward, $ZnWO_4$ downward), the formation of depletion layers, and the establishment of a built-in electric field at the interface. Furthermore, under light illumination, the Cu-BTC/$ZnWO_4$ heterostructure experienced excitation, causing the band edges to bend and the built-in electric field, along with Coulombic force interaction, facilitated the rapid migration of excited e^- in the CB of

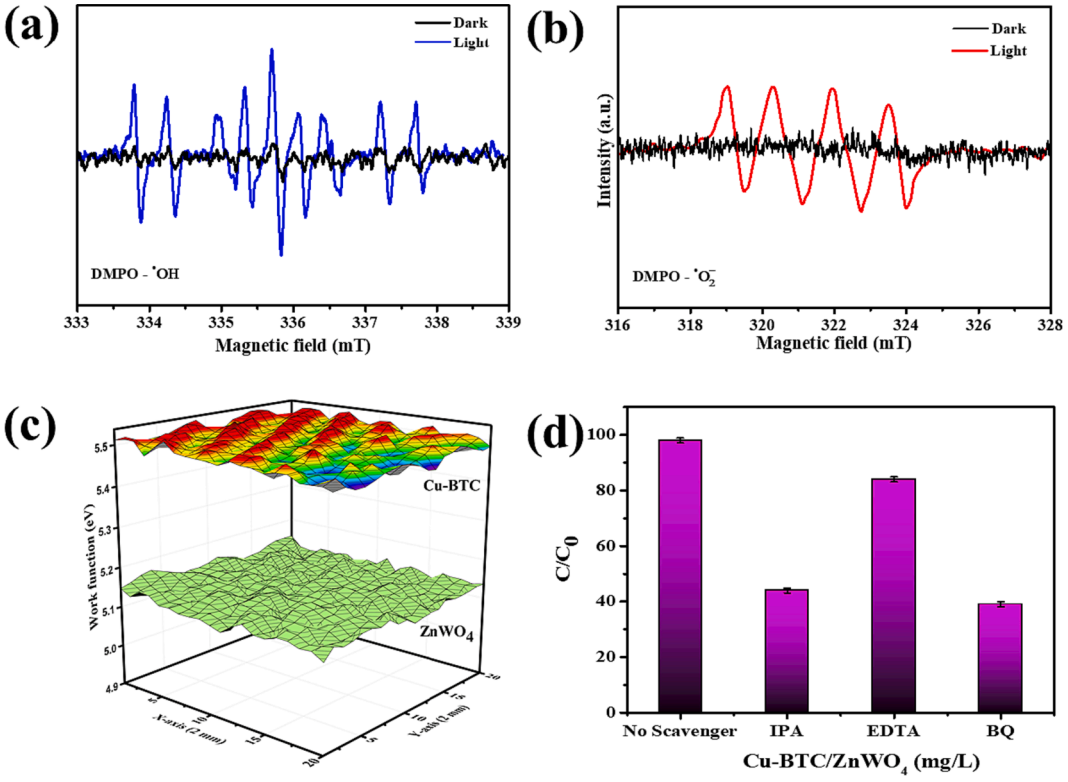

Fig. 6. (a-b). ESR spectra of Cu-BTC/$ZnWO_4$ heterostructure for •OH, and $O_2^{•-}$ under dark and irradiation, respectively. (c) work function of Cu-BTC/$ZnWO_4$ heterostructure (d) Sonophotocatalytic TC degradation in presence of various radical scavengers over Cu-BTC/$ZnWO_4$ heterostructure.

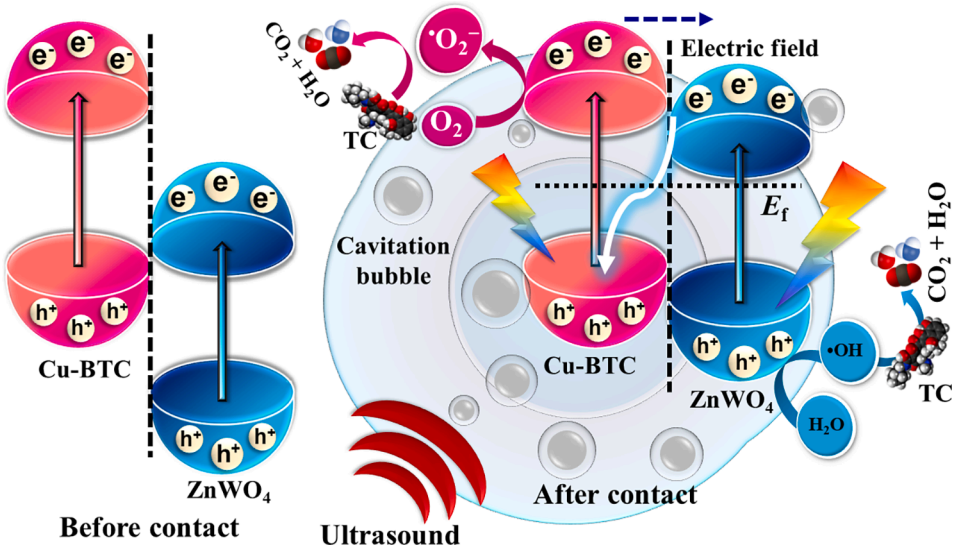

Fig. 7. Schematic illustration depicting the degradation of TC using sonophotocatalysis on Cu-BTC/$ZnWO_4$ S-scheme photocatalysts.

$ZnWO_4$ across the interfaces to recombine with h^+ in the VB of Cu-BTC. As a result, the accumulated electrons in the CB of Cu-BTC and h^+ in the VB of $ZnWO_4$ were retained and actively participated in the reduction of O_2 to $\bullet O_2^-$ and oxidation of adsorbed H_2O to generate •OH, respectively. Additionally, the fabricated Cu-BTC/$ZnWO_4$ heterostructure provided additional nuclei for the formation and growth of cavitation bubbles in a liquid, thereby enhancing acoustic cavitation. Notably, the collapse of these cavitation bubbles generated a significant amount of heat energy, which increased the pyrolysis ratio of H_2O molecules. This energetic process led to the production of ROS through the "hot spot" mechanism. The ROS molecules then attacked TC molecules, causing mineralization into smaller molecules. However, the sole action of ultrasonic irradiation was insufficient for TC degradation due to the significant loss of ROS before reaching TC. Moreover, the ultrasonication process continuously refreshed the surface area and active sites of the Cu-BTC/$ZnWO_4$ heterostructure by eliminating any degradation intermediates through mass transfer in the sonophotocatalytic strategy. Furthermore, the improved efficiency of e^-/h^+ pair transfer and separation in the Cu-BTC/

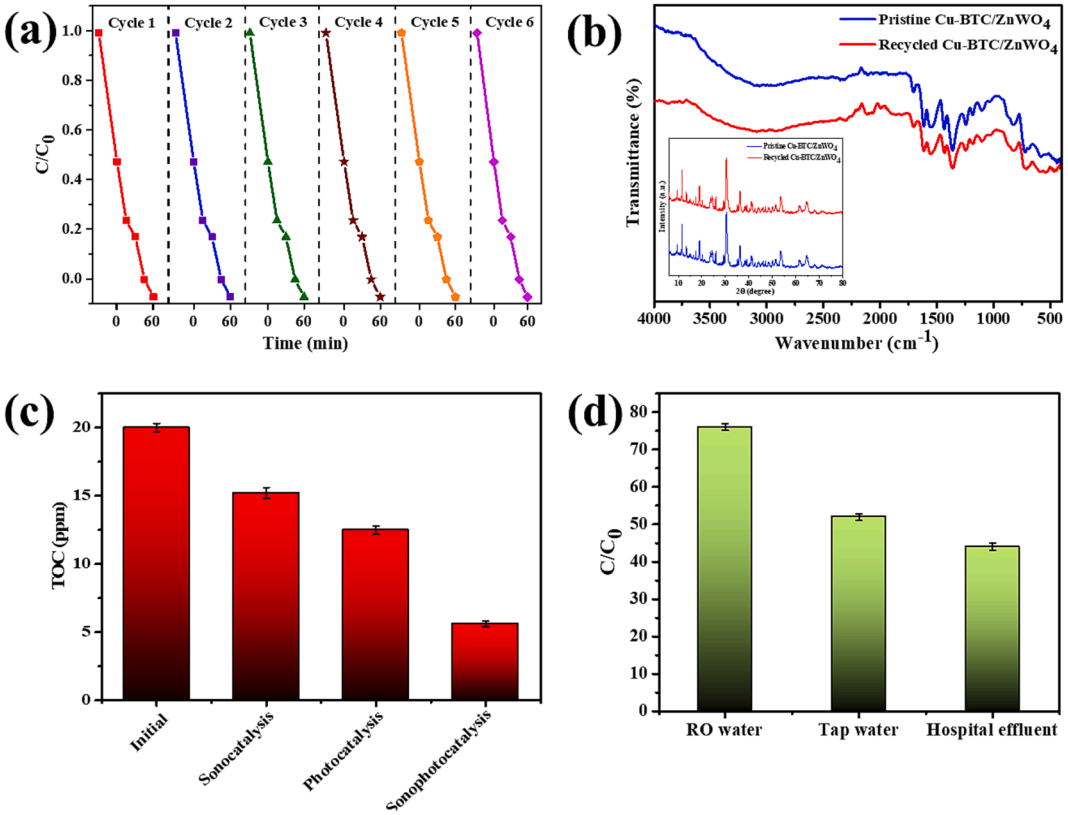

Fig. 8. (a) Repetitive cycles of sonophotocatalytic TC degradation. (b) XRD and FT-IR spectra of pristine photocatalyst after 6 cycles of degradation. (c) Mineralization of TOC under sonocatalysis, photocatalysis and sonophotocatalysis. (d) Sonophotocatalytic TC degradation over Cu-BTC/$ZnWO_4$ heterostructure in different matrices, including RO water, tap water, and hospital effluent.

$ZnWO_4$ heterostructure was attributed to the matched band edge potentials of Cu-BTC and $ZnWO_4$.

3.5. Stability and reusability of Cu-BTC/$ZnWO_4$

The long-term stability and recyclability of photoactive materials are critical factors for their practical application in real-time and cost-effective scenarios. To assess the reusability of Cu-BTC/$ZnWO_4$, six successive cycles of TC degradation were conducted under identical reaction conditions. The impact of cycle numbers on the sonophotocatalytic degradation efficiency of TC is presented in Fig. 8a. After each cycle, the used Cu-BTC/$ZnWO_4$ catalyst was separated from the solution via centrifugation, cleaned with a mixture of deionized water and ethanol, and dried at 60 °C for approximately 3–4 h. The regenerated heterostructure was then employed in subsequent runs.

The developed material demonstrated remarkable potential for reuse even after six consecutive cycles. The stability of the material was further confirmed through FT-IR and XRD analyses, comparing the characteristics of Cu-BTC/$ZnWO_4$ before and after the consecutive TC degradation cycles (Fig. 8b). The results revealed no significant variations in peak positions, indicating the preservation of the material's stable structure even after six consecutive sonophotocatalytic degradation and regeneration cycles. Fig. 8c demonstrates the percentage of total organic carbon (TOC) removal after the sonophotocatalytic degradation of TC. The findings indicate that after 60 min of sonophotocatalytic treatment, around 72 % of the TOC was eliminated. In comparison, sonocatalytic and photocatalytic treatments only achieved 24 % and 38 % mineralization, respectively. These results demonstrate the significant potential of the Cu-BTC/$ZnWO_4$ heterostructure for effectively mineralizing industrial wastewater.

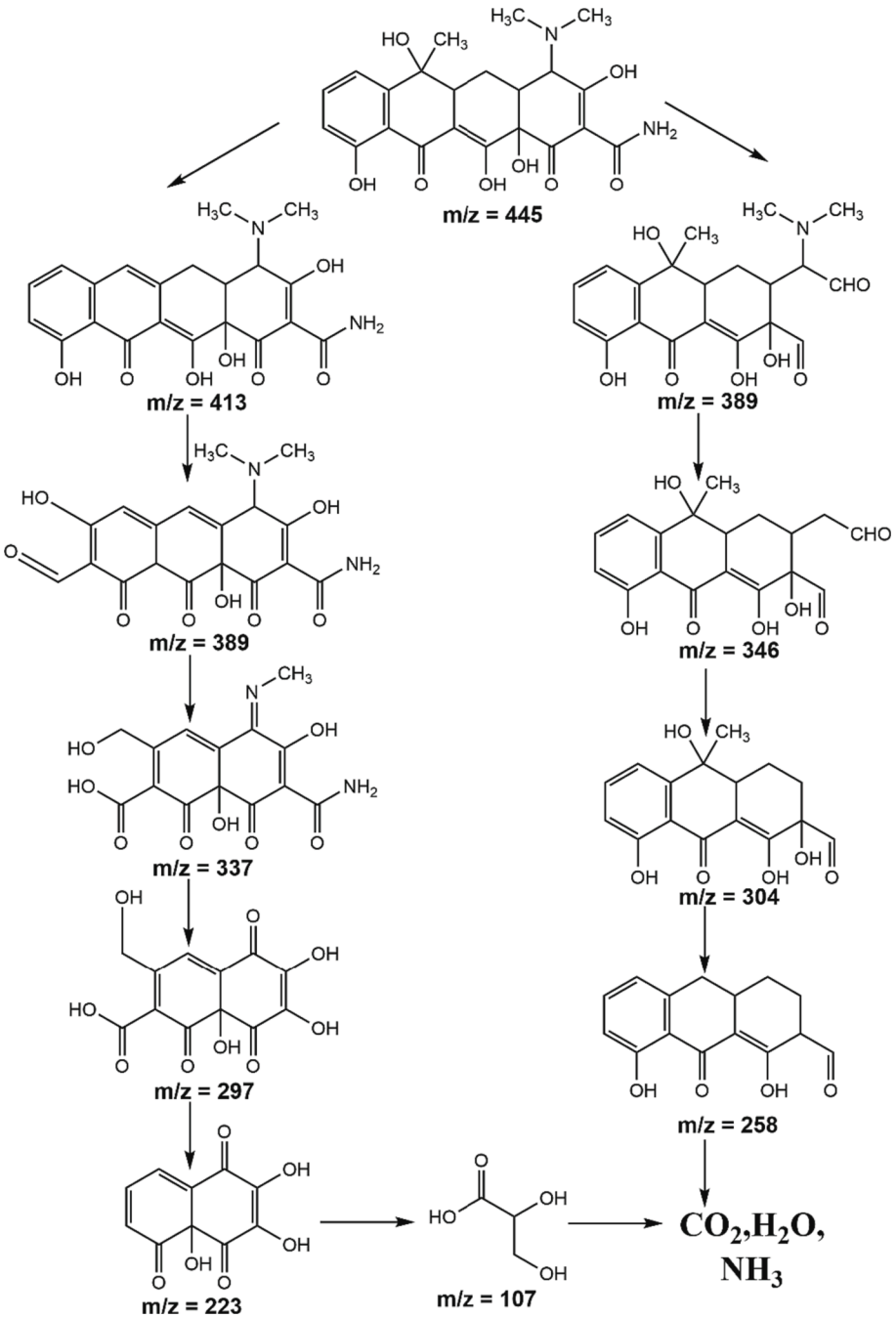

Fig. 9. Possible TC mineralization pathway over Cu-BTC/$ZnWO_4$ heterostructure.

To investigate the impact of different water matrices on the sonophotocatalytic performance of Cu-BTC/$ZnWO_4$, various water samples including RO water, tap water, and real water samples from hospital effluent were collected and their characteristics were detailed in **Table S2**. As depicted in Fig. 8d, the sonophotocatalytic degradation of TC exhibited rapid progress when using RO water, achieving a removal efficiency of 76 %. Conversely, the degradation performances in tap water (52 %) and hospital effluent (44 %) were comparatively lower than that observed with RO water. This disparity can likely be attributed to the presence of additional contaminants in the real water samples [79]. Hospital effluent, in particular, contains a diverse range of organic and inorganic compounds, including pharmaceuticals [80,81]. The presence of these various compounds and their interactions can impact the efficiency of sonophotocatalysis. Certain compounds may exhibit greater resistance to degradation or compete with the target compounds for adsorption and reaction sites on the surface of the photocatalyst [82].

To understand the impact of intermediate products on the effectiveness of contaminant mineralization, it is crucial to identify the potential degradation pathways of TC into simpler components like CO_2, H_2O, and other low molecular weight mineralized products. The breakdown of tetracycline molecules occurs through the attack of various ROS generated during the sonophotocatalytic processes. Typically, tetracycline degradation during sonophotocatalysis involves the breakdown of double bonds, phenolic groups, N-dimethyl groups, and the amine group of the tetracycline molecule. These functional groups and electron-rich positions are susceptible to attack by active radicals such as $\bullet O_2^-$, OH•, h^+, and H_2O_2. Based on the results obtained from LC-MS analysis (**S3 and Fig. S5**), plausible routes for the sonophotocatalytic mineralization of TC have been proposed (Fig. 9).

Before the reaction, the single peak of TC had a mass-to-charge ratio (m/z) of 445. After 30 min of sonophotocatalytic degradation, the TC peak signal decreased, and new products with m/z values of 445, 413, 389, 346, 337, 297, and 223 appeared. These products likely formed through processes such as N-demethylation, hydroxylation, and dehydroxylation. After 60 min of sonophotocatalysis, the single peak m/z 445 of TC completely disappeared, and fragmented products with m/z values of 304, 297, 223, and 107 were observed. Two possible degradation pathways of tetracycline during sonophotocatalysis can be proposed: First pathway: The double bond between C2 and C13 of TC attacked by h^+, inducing the cleavage of double bond. This leads to the formation of amino-free intermediate compounds (m/z = 389). The removal of -N$(CH_3)_2$-CHO, dihydroxylation and demethylation forms the intermediate products (m/z = 346, 304, 258), which further mineralizes into small molecule fragments. Second pathway: The attack on the C-N bond of TC is another possible degradation route of tetracycline during sonophotocatalysis. Substitution of –OH group results in the formation of intermediate compound (m/z = 389). Detachment of benzene ring from the previously formed intermediate leads to the generation of (m/z = 337). Further attack by free radicals transforms to (m/z = 297, 223 and 107). Eventually, all intermediates are decomposed into inorganic substances.

4. Conclusions

By combining Cu-BTC with $ZnWO_4$, a novel approach was used to achieve an improved sonophotocatalytic performance. The resulting coupled catalyst exhibited several enhancements, including enhanced light absorption, narrow bandgap, and improved conductivity, confirmed through optical and electrochemical analyses. These improvements led to efficient separation of e^-/h^+ pairs and a reduced recombination rate of charge carriers, indicating a significant enhancement in sonophotocatalytic activity (98 %). Additionally, the formation of an S-scheme heterojunction between Cu-BTC and $ZnWO_4$ played a crucial role in enhancing the catalyst's sonophotocatalytic activity. This heterojunction facilitated electron migration within the catalyst, particularly under irradiation, thereby enhancing its performance. The improved sonophotocatalytic activity of the Cu-BTC/$ZnWO_4$ heterostructure was further demonstrated by the generation of highly reactive species, such as •OH and h^+, during the degradation of TC molecules. This was confirmed through ESR analysis and scavenger tests. To gain a better understanding of the degradation process, various operational parameters were carefully optimized and applied in subsequent experiments. Furthermore, LC-MS analysis was employed to propose potential pathways for the destruction of TC molecules during the sonophotocatalytic treatment. These findings emphasize the significant role played by the S-scheme heterojunction mechanism in enhancing the sonophotocatalytic activity of the Cu-BTC/$ZnWO_4$ heterostructure. The optimised catalyst improved the performance, along with its ability to generate reactive species and its potential for degrading TC, makes it promising candidate for the effective removal of persistent emerging pollutants in water.

CRediT authorship contribution statement

Jenson Samraj Jeyaprakash: Conceptualization, Methodology, Validation, Investigation, Data curation, Writing – original draft. **Manju Rajamani:** Methodology, Validation, Investigation, Data curation, Software. **Claudia L. Bianchi:** Validation, Investigation. **Muthupandian Ashokkumar:** Data curation, Software. **Bernaurdshaw Neppolian:** Funding acquisition, Resources, Supervision, Writing – review & editing.

Declaration of Competing Interest

The authors declare that they have no known competing financial interests or personal relationships that could have appeared to influence the work reported in this paper.

Data availability

Data will be made available on request.

Acknowledgements

The authors gratefully acknowledge the Department of Science and Technology – Water Technology Initiative (DST-WTI) [File No: DST/TMD/EWO/WTI/2K19/EWFH/2019/169] for their financial support. Jenson Samraj Jeyaprakash is supported by the INSPIRE fellowship (DST/INSPIRE Fellowship/[IF210538]) from the Department of Science and Technology, Government of India.

Appendix A. Supplementary data

Supplementary data to this article can be found online at https://doi.org/10.1016/j.ultsonch.2023.106624.

References

[1] G. Chaturvedi, A. Kaur, A. Umar, M.A. Khan, H. Algarni, S.K. Kansal, Removal of fluoroquinolone drug, levofloxacin, from aqueous phase over iron based MOFs, MIL-100(Fe), J. Solid State Chem. 281 (2020), 121029, https://doi.org/10.1016/j.jssc.2019.121029.

[2] F.-A. Weber, T. Aus Der Beek, A. Carius, G. Grüttner, S. Hickmann, I. Ebert, A. Hein, A. Küster, J. Rose, J. Koch-Jugl, Pharmaceuticals in the environment-the global perspective Occurrence, effects, and potential cooperative action under SAICM, (2014). www.umweltbundesamt.de/umweltbundesamt.de/umweltbundesamt (accessed May 5, 2023).

[3] S. Comber, M. Gardner, P. Sörme, D. Leverett, B. Ellor, Active pharmaceutical ingredients entering the aquatic environment from wastewater treatment works: A cause for concern? Sci. Total Environ. 613–614 (2018) 538–547, https://doi.org/10.1016/J.SCITOTENV.2017.09.101.

[4] M.C. Shutter, H. Akhondi, Tetracycline, Kucers Use Antibiot. A Clin. Rev. Antibacterial, Antifung. Antiparasit. Antivir. Drugs, Seventh Ed. (2022) 1195–1203. https://doi.org/10.1201/9781315152110.

[5] S.Y. Hashemi, M. Yegane Badi, H. Pasalari, A. Azari, H. Arfaeinia, A. Kiani, Degradation of Ceftriaxone from aquatic solution using a heterogeneous and

reusable O3/UV/ Fe3O4@TiO2 systems: operational factors, kinetics and mineralisation, Https://Doi.Org/10.1080/03067319.2020.1817909. 102 (2020) 6904–6920. https://doi.org/10.1080/03067319.2020.1817909.
[6] M. Gheytanzadeh, A. Baghban, S. Habibzadeh, K. Jabbour, A. Esmaeili, A. Mohaddespour, O. Abida, An insight into tetracycline photocatalytic degradation by MOFs using the artificial intelligence technique, Sci. Reports 2022 121. 12 (2022) 1–11. https://doi.org/10.1038/s41598-022-10563-8.
[7] L. Hu, J. Chen, Y. Wei, M. Wang, Y. Xu, C. Wang, P. Gao, Y. Liu, C. Liu, Y. Song, N. Ding, X. Liu, R. Wang, Photocatalytic degradation effect and mechanism of Karenia mikimotoi by non-noble metal modified TiO2 loading onto copper metal organic framework (SNP-TiO2@Cu-MOF) under visible light, J. Hazard. Mater. 442 (2023), 130059, https://doi.org/10.1016/j.jhazmat.2022.130059.
[8] H.Q. Ha, H.T.D. Nguyen, T.H.M. Pham, V.T. Pham, T. Truong, Towards optical application of metal-organic frameworks: Cu-MOFs as sole heterogeneous photocatalyst for arylation of phenols at room temperature, Catal. Commun. 117 (2018) 79–84, https://doi.org/10.1016/j.catcom.2018.08.030.
[9] C. Brahmi, M. Benltifa, C. Vaulot, L. Michelin, F. Dumur, F. Millange, M. Frigoli, A. Airoudj, F. Morlet-Savary, L. Bousselmi, J. Lalevée, New hybrid MOF/polymer composites for the photodegradation of organic dyes, Eur. Polym. J. 154 (2021), 110560, https://doi.org/10.1016/j.eurpolymj.2021.110560.
[10] W. Cheng, X. Tang, Y. Zhang, D. Wu, W. Yang, Applications of metal-organic framework (MOF)-based sensors for food safety: Enhancing mechanisms and recent advances, Trends Food Sci. Technol. 112 (2021) 268–282, https://doi.org/10.1016/j.tifs.2021.04.004.
[11] H. Sohrabi, S. Ghasemzadeh, Z. Ghoreishi, M.R. Majidi, Y. Yoon, N. Dizge, A. Khataee, Metal-organic frameworks (MOF)-based sensors for detection of toxic gases: A review of current status and future prospects, Mater. Chem. Phys. 299 (2023), 127512, https://doi.org/10.1016/j.matchemphys.2023.127512.
[12] R. Kaur, A. Kaur, R. Kaur, S. Singh, M.S. Bhatti, A. Umar, S. Baskoutas, S.K. Kansal, Cu-BTC metal organic framework (MOF) derived Cu-doped TiO2 nanoparticles and their use as visible light active photocatalyst for the decomposition of ofloxacin (OFX) antibiotic and antibacterial activity, Adv. Powder Technol. 32 (2021) 1350–1361, https://doi.org/10.1016/j.apt.2021.02.037.
[13] M. Yazdani-Aval, S. Alizadeh, A. Bahrami, D. Nematollahi, F. Ghorbani-Shahna, Efficient removal of gaseous toluene by the photoreduction of Cu/Zn-BTC metal-organic framework under visible-light, Optik (stuttg). 247 (2021), 167841, https://doi.org/10.1016/j.ijleo.2021.167841.
[14] M.S. Samuel, K.V. Savunthari, S. Ethiraj, Synthesis of a copper (II) metal–organic framework for photocatalytic degradation of rhodamine B dye in water, Environ. Sci. Pollut. Res. 28 (2021) 40835–40843, https://doi.org/10.1007/s11356-021-13571-9.
[15] Y. Wu, X. Li, H. Zhao, F. Yao, J. Cao, Z. Chen, D. Wang, Q. Yang, Core-shell structured Cu2O@HKUST-1 heterojunction photocatalyst with robust stability for highly efficient tetracycline hydrochloride degradation under visible light, Chem. Eng. J. 426 (2021), 131255, https://doi.org/10.1016/j.cej.2021.131255.
[16] H. Yu, H. Yin, L. Wang, S. Zhao, J. Gong, Z. Ji, Y. Zheng, Q. Nie, Construction of MOFs-based AgI/Ag/Cu3(BTC)2 ternary composites as Z-scheme photocatalysts for effective degradation of tetracycline, Bull. Mater. Sci. 44 (2021) 127, https://doi.org/10.1007/s12034-021-02414-5.
[17] V. Vinesh, M. Preeyanghaa, T.R.N. Kumar, M. Ashokkumar, C.L. Bianchi, B. Neppolian, Revealing the stability of CuWO4/g-C3N4 nanocomposite for photocatalytic tetracycline degradation from the aqueous environment and DFT analysis, Environ. Res. 207 (2022), 112112, https://doi.org/10.1016/j.envres.2021.112112.
[18] K. Qureshi, M.Z. Ahmad, I.A. Bhatti, M. Zahid, J. Nisar, M. Iqbal, Graphene oxide decorated ZnWO4 architecture synthesis, characterization and photocatalytic activity evaluation, J. Mol. Liq. 285 (2019) 778–789, https://doi.org/10.1016/j.molliq.2019.04.139.
[19] G. Kumar, I. Mukherjee, M. Dubey, B.P. Vellenki, R.K. Dutta, Photocatalytic degradation of tetracycline in aqueous medium using ZnWO4/Bi2MoO6 nanocomposites under natural sunlight, Int. J. Environ. Sci. Technol. 20 (2023) 2903–2918, https://doi.org/10.1007/s13762-022-04047-5.
[20] Q. Xu, L. Zhang, B. Cheng, J. Fan, J. Yu, S-Scheme heterojunction photocatalyst, Chem. 6 (2020) 1543–1559, https://doi.org/10.1016/j.chempr.2020.06.010.
[21] A.R.M. Shaheer, V. Vinesh, S.K. Lakhera, B. Neppolian, Reduced graphene oxide as a solid-state mediator in TiO2/In0.5WO3 S-scheme photocatalyst for hydrogen production, Sol. Energy 213 (2021) 260–270, https://doi.org/10.1016/j.solener.2020.11.030.
[22] M. Preeyanghaa, V. Vinesh, B. Neppolian, Construction of S-scheme 1D/2D rod-like g-C3N4/V2O5 heterostructure with enhanced sonophotocatalytic degradation for Tetracycline antibiotics, Chemosphere 287 (2022), 132380, https://doi.org/10.1016/j.chemosphere.2021.132380.
[23] T. Wu, Q. Liang, L. Tang, J. Tang, J. Wang, B. Shao, S. Gong, Q. He, Y. Pan, Z. Liu, Construction of a novel S-scheme heterojunction piezoelectric photocatalyst V-BiOIO3/FTCN and immobilization with floatability for tetracycline degradation, J. Hazard. Mater. 443 (2023), 130251, https://doi.org/10.1016/j.jhazmat.2022.130251.
[24] J. Zhang, Y. Zhao, K. Zhang, A. Zada, K. Qi, Sonocatalytic degradation of tetracycline hydrochloride with CoFe2O4/g-C3N4 composite, Ultrason. Sonochem. 94 (2023), 106325, https://doi.org/10.1016/j.ultsonch.2023.106325.
[25] K. Zhang, J. Zhang, X. He, Y. Zhao, A. Zada, A. Peng, K. Qi, Fe3O4@MIL-100(Fe) modified ZnS nanoparticles with enhanced sonocatalytic degradation of tetracycline antibiotic in water, Ultrason. Sonochem. 95 (2023), 106409, https://doi.org/10.1016/j.ultsonch.2023.106409.
[26] J. Zhang, X. Gu, Y. Zhao, K. Zhang, Y. Yan, K. Qi, Photocatalytic Hydrogen Production and Tetracycline Degradation Using ZnIn2S4 Quantum Dots Modified g-C3N4 Composites, Nanomaterials 13 (2023) 305, https://doi.org/10.3390/nano13020305.
[27] Q. Cui, X. Gu, Y. Zhao, K. Qi, Y. Yan, S-scheme CuInS2/ZnS heterojunctions for the visible light-driven photocatalytic degradation of tetracycline antibiotic drugs, J. Taiwan Inst. Chem. Eng. 142 (2023), 104679, https://doi.org/10.1016/j.jtice.2023.104679.
[28] K. Qi, C. Zhuang, M. Zhang, P. Gholami, A. Khataee, Sonochemical synthesis of photocatalysts and their applications, J. Mater. Sci. Technol. 123 (2022) 243–256, https://doi.org/10.1016/j.jmst.2022.02.019.
[29] C. Cheng, B. He, J. Fan, B. Cheng, S. Cao, J. Yu, An Inorganic/Organic S-Scheme Heterojunction H 2 -Production Photocatalyst and its Charge Transfer Mechanism, Adv. Mater. 33 (2021), https://doi.org/10.1002/adma.202100317.
[30] P. Xia, S. Cao, B. Zhu, M. Liu, M. Shi, J. Yu, Y. Zhang, Designing a 0D/2D S-Scheme Heterojunction over Polymeric Carbon Nitride for Visible-Light Photocatalytic Inactivation of Bacteria, Angew. Chemie Int. Ed. 59 (2020) 5218–5225, https://doi.org/10.1002/anie.201916012.
[31] B. He, Z. Wang, P. Xiao, T. Chen, J. Yu, L. Zhang, Cooperative Coupling of H 2 O 2 Production and Organic Synthesis over a Floatable Polystyrene-Sphere-Supported TiO 2 /Bi 2 O 3 S-Scheme Photocatalyst, Adv. Mater. 34 (2022), https://doi.org/10.1002/adma.202203225.
[32] B. Zhu, Q. Dong, J. Huang, M. Yang, X. Chen, C. Zhai, Q. Chen, B. Wang, H. Tao, L. Chen, Self-Assembly of Bi 2 Sn 2 O 7 /β-Bi 2 O 3 S-Scheme Heterostructures for Efficient Visible-Light-Driven Photocatalytic Degradation of Tetracycline, ACS Omega 8 (2023) 13702–13714, https://doi.org/10.1021/acsomega.2c07899.
[33] B. Venu, V. Shirisha, B. Vishali, G. Naresh, R. Kishore, I. Sreedhar, A. Venugopal, A Cu-BTC metal–organic framework (MOF) as an efficient heterogeneous catalyst for the aerobic oxidative synthesis of imines from primary amines under solvent free conditions, New J. Chem. 44 (2020) 5972–5979, https://doi.org/10.1039/C9NJ05997K.
[34] C. Zhang, H. Zhang, K. Zhang, X. Li, Q. Leng, C. Hu, Photocatalytic activity of ZnWO4: Band structure, morphology and surface modification, ACS Appl. Mater. Interfaces 6 (2014) 14423–14432, https://doi.org/10.1021/AM503696B/ASSET/IMAGES/MEDIUM/AM-2014-03696B_0008.GIF.
[35] S. Bouson, A. Krittayavathananon, N. Phattharasupakun, P. Siwayaprahm, M. Sawangphruk, Antifungal activity of water-stable copper-containing metal-organic frameworks, R. Soc. Open Sci. 4 (2017), 170654, https://doi.org/10.1098/rsos.170654.
[36] S.-M. Hwang, S.Y. Choi, M.H. Youn, W. Lee, K.T. Park, K. Gothandapani, A. N. Grace, S.K. Jeong, Investigation on Electroreduction of CO 2 to Formic Acid Using Cu 3 (BTC) 2 Metal-Organic Framework (Cu-MOF) and Graphene Oxide, ACS Omega 5 (2020) 23919–23930, https://doi.org/10.1021/acsomega.0c03170.
[37] M. Zhong, S. Zhang, A. Dong, Z. Sui, L. Feng, Q. Chen, Cu-MOF/Au–Pd composite catalyst: preparation and catalytic performance evaluation, J. Mater. Sci. 55 (2020) 10388–10398, https://doi.org/10.1007/s10853-020-04699-z.
[38] M.R. Tamtam, R. Koutavarapu, J. Shim, InVO4 nanosheets decorated with ZnWO4 nanorods: A novel composite and its enhanced photocatalytic performance under solar light, Environ. Res. 227 (2023), 115735, https://doi.org/10.1016/j.envres.2023.115735.
[39] Y.A. Sethi, C.S. Praveen, R.P. Panmand, A. Ambalkar, A.K. Kulkarni, S.W. Gosavi, M.V. Kulkarni, B.B. Kale, Perforated N-doped monoclinic ZnWO 4 nanorods for efficient photocatalytic hydrogen generation and RhB degradation under natural sunlight, Catal, Sci. Technol. 8 (2018) 2909–2919, https://doi.org/10.1039/C8CY00521D.
[40] M. Rajamani, A. Rajan, B. Neppolian, Photocatalytic pathway toward real time control of tetracycline from industrial wastewater mediated by hetero-structure CuFe2O4-SnS2, J. Environ. Chem. Eng. 11 (2023), 109129, https://doi.org/10.1016/j.jece.2022.109129.
[41] B.M. Omkaramurthy, G. Krishnamurthy, S. Foro, Synthesis and characterization of mesoporous crystalline copper metal–organic frameworks for electrochemical energy storage application, SN Appl. Sci. 2 (2020) 342, https://doi.org/10.1007/s42452-020-2051-6.
[42] W.S.A. El-Yazeed, A.I. Ahmed, Monometallic and bimetallic Cu–Ag MOF/MCM-41 composites: structural characterization and catalytic activity, RSC Adv. 9 (2019) 18803–18813, https://doi.org/10.1039/C9RA03310F.
[43] Y.A. Sethi, C.S. Praveen, R.P. Panmand, A. Ambalkar, A.K. Kulkarni, S.W. Gosavi, M.V. Kulkarni, B.B. Kale, Perforated N-doped monoclinic ZnWO4 nanorods for efficient photocatalytic hydrogen generation and RhB degradation under natural sunlight, Catal, Sci. Technol. 8 (2018) 2909–2919, https://doi.org/10.1039/c8cy00521d.
[44] S.A. Siddiqui, A. Prado-Roller, H. Shiozawa, Room temperature synthesis of a luminescent crystalline Cu–BTC coordination polymer and metal–organic framework, Mater. Adv. 3 (2022) 224–231, https://doi.org/10.1039/D1MA00866H.
[45] Y. Wu, J. Zhang, B. Long, H. Zhang, The Thermodynamic Stability, Electronic and Photocatalytic Properties of the ZnWO 4 (100) Surface as Predicted by Screened Hybrid Density Functional Theory, ACS Omega 6 (2021) 15057–15067, https://doi.org/10.1021/acsomega.1c01214.
[46] H.L. Abubakar, J.O. Tijani, S.A. Abdulkareem, A. Mann, S. Mustapha, A review on the applications of zinc tungstate (ZnWO4) photocatalyst for wastewater treatment, Heliyon. 8 (2022) e09964.
[47] J. Zhao, X. Yan, N. Zhao, X. Li, B. Lu, X. Zhang, H. Yu, Cocatalyst designing: a binary noble-metal-free cocatalyst system consisting of ZnIn 2 S 4 and In(OH) 3 for efficient visible-light photocatalytic water splitting, RSC Adv. 8 (2018) 4979–4986, https://doi.org/10.1039/C7RA12586K.

[48] B. Sarma, S.K. Deb, B.K. Sarma, Photoluminescence and photocatalytic activities of Ag/ZnO metal-semiconductor heterostructure, J. Phys. Conf. Ser. 765 (2016), 012023, https://doi.org/10.1088/1742-6596/765/1/012023.
[49] S. Phanichphant, A. Nakaruk, K. Chansaenpak, D. Channei, Evaluating the photocatalytic efficiency of the BiVO4/rGO photocatalyst, Sci. Rep. 9 (2019) 16091, https://doi.org/10.1038/s41598-019-52589-5.
[50] H.Y. Hafeez, S.K. Lakhera, S. Bellamkonda, G.R. Rao, M.V. Shankar, D. W. Bahnemann, B. Neppolian, Construction of ternary hybrid layered reduced graphene oxide supported g-C 3 N 4 -TiO 2 nanocomposite and its photocatalytic hydrogen production activity, Int. J. Hydrogen Energy 43 (2018) 3892–3904, https://doi.org/10.1016/j.ijhydene.2017.09.048.
[51] R. Vinoth, P. Karthik, K. Devan, B. Neppolian, M. Ashokkumar, TiO2–NiO p–n nanocomposite with enhanced sonophotocatalytic activity under diffused sunlight, Ultrason. Sonochem. 35 (2017) 655–663, https://doi.org/10.1016/j.ultsonch.2016.03.005.
[52] K. Yun, K. Saravanakumar, G. Jagan, Y. Yea, Y. Yoon, C.M. Park, Fabrication of highly effective Ag6Si2O7/SmFeO3 heterojunction with synergistically enhanced sonophotocatalytic degradation of ciprofloxacin and production of H2O2: Influencing factors and degradation mechanism, Chem. Eng. J. 468 (2023), 143491, https://doi.org/10.1016/j.cej.2023.143491.
[53] P. Liu, Z. Wu, A.V. Abramova, G. Cravotto, Sonochemical processes for the degradation of antibiotics in aqueous solutions: A review, Ultrason. Sonochem. 74 (2021), 105566, https://doi.org/10.1016/j.ultsonch.2021.105566.
[54] R. James Wood, T. Sidnell, I. Ross, J. McDonough, J. Lee, M.J. Bussemaker, Ultrasonic degradation of perfluorooctane sulfonic acid (PFOS) correlated with sonochemical and sonoluminescence characterisation, Ultrason. Sonochem. 68 (2020), 105196, https://doi.org/10.1016/j.ultsonch.2020.105196.
[55] J. Choi, Y. Son, Effect of dissolved gases on sonochemical oxidation in a 20 kHz probe system: Continuous monitoring of dissolved oxygen concentration and sonochemical oxidation activity, Ultrason. Sonochem. 97 (2023), 106452, https://doi.org/10.1016/j.ultsonch.2023.106452.
[56] S. Haddadi, A. Khataee, S. Arefi-Oskoui, B. Vahid, Y. Orooji, Y. Yoon, Titanium-based MAX-phase with sonocatalytic activity for degradation of oxytetracycline antibiotic, Ultrason. Sonochem. 92 (2023), 106255, https://doi.org/10.1016/j.ultsonch.2022.106255.
[57] E. Kuna, R. Behling, S. Valange, G. Chatel, J.C. Colmenares, Sonocatalysis: A Potential Sustainable Pathway for the Valorization of Lignocellulosic Biomass and Derivatives, Top. Curr. Chem. 375 (2017) 41, https://doi.org/10.1007/s41061-017-0122-y.
[58] M.H. Abdurahman, A.Z. Abdullah, N.F. Shoparwe, A comprehensive review on sonocatalytic, photocatalytic, and sonophotocatalytic processes for the degradation of antibiotics in water: Synergistic mechanism and degradation pathway, Chem. Eng. J. 413 (2021), 127412, https://doi.org/10.1016/j.cej.2020.127412.
[59] L. Zeng, S. Li, X. Li, J. Li, S. Fan, X. Chen, Z. Yin, M. Tadé, S. Liu, Visible-light-driven sonophotocatalysis and peroxymonosulfate activation over 3D urchin-like MoS2/C nanoparticles for accelerating levofloxacin elimination: Optimization and kinetic study, Chem. Eng. J. 378 (2019), 122039, https://doi.org/10.1016/j.cej.2019.122039.
[60] M. Preeyanghaa, E.S. Erakulan, R. Thapa, M. Ashokkumar, B. Neppolian, Scrutinizing the role of tunable carbon vacancies in g-C3N4 nanosheets for efficient sonophotocatalytic degradation of Tetracycline in diverse water matrices: Experimental study and theoretical calculation, Chem. Eng. J. 452 (2023), 139437, https://doi.org/10.1016/j.cej.2022.139437.
[61] R.E. Nimshi, J.J. Vijaya, L.J. Kennedy, P.S. Selvamani, M. Bououdina, P.J. Sophia, Effective microwave assisted synthesis of CoFe2O4@TiO2@rGO ternary nanocomposites for the synergic sonophotocatalytic degradation of tetracycline and c antibiotics, Ceram. Int. 49 (2023) 13762–13773, https://doi.org/10.1016/j.ceramint.2022.12.254.
[62] S.R. Yashas, H.P. Shivaraju, T. Thinley, K.S. Pushparaj, A. Maleki, B. Shahmoradi, Facile synthesis of SnO2 2D nanoflakes for ultrasound-assisted photodegradation of tetracycline hydrochloride, Int. J. Environ. Sci. Technol. 17 (2020) 2593–2604, https://doi.org/10.1007/s13762-020-02636-w.
[63] A. Bembibre, M. Benamara, M. Hjiri, E. Gómez, H.R. Alamri, R. Dhahri, A. Serrà, Visible-light driven sonophotocatalytic removal of tetracycline using Ca-doped ZnO nanoparticles, Chem. Eng. J. 427 (2022), 132006, https://doi.org/10.1016/j.cej.2021.132006.
[64] R. Abazari, A.R. Mahjoub, S. Sanati, Z. Rezvani, Z. Hou, H. Dai, Ni–Ti Layered Double Hydroxide@Graphitic Carbon Nitride Nanosheet: A Novel Nanocomposite with High and Ultrafast Sonophotocatalytic Performance for Degradation of Antibiotics, Inorg. Chem. 58 (2019) 1834–1849, https://doi.org/10.1021/acs.inorgchem.8b02575.
[65] A. Esmaeili, S. Pourranjabar Hasan Kiadeh, A. Ebrahimian Pirbazari, F. Esmaeili Khalil Saraei, A. Ebrahimian Pirbazari, A. Derakhshesh, F.-S. Tabatabai-Yazdi, CdS nanocrystallites sensitized ZnO nanosheets for visible light induced sonophotocatalytic/photocatalytic degradation of tetracycline: From experimental results to a generalized model based on machine learning methods, Chemosphere. 332 (2023) 138852. https://doi.org/10.1016/j.chemosphere.2023.138852.
[66] A. Khataee, T. Sadeghi Rad, S. Nikzat, A. Hassani, M.H. Aslan, M. Kobya, E. Demirbaş, Fabrication of NiFe layered double hydroxide/reduced graphene oxide (NiFe-LDH/rGO) nanocomposite with enhanced sonophotocatalytic activity for the degradation of moxifloxacin, Chem. Eng. J. 375 (2019), 122102, https://doi.org/10.1016/j.cej.2019.122102.
[67] G. Fan, C. Cai, S. Yang, B. Du, J. Luo, Y. Chen, X. Lin, X. Li, Y. Wang, Sonophotocatalytic degradation of ciprofloxacin by Bi2MoO6/FeVO4 heterojunction: Insights into performance, mechanism and pathway, Sep. Purif. Technol. 303 (2022), 122251, https://doi.org/10.1016/j.seppur.2022.122251.
[68] T.J. Al-Musawi, N. Mengelizadeh, K. Sathishkumar, S. Mohebi, D. Balarak, Preparation of CuFe2O4/montmorillonite nanocomposite and explaining its performance in the sonophotocatalytic degradation process for ciprofloxacin, Colloid Interface Sci. Commun. 45 (2021), 100532, https://doi.org/10.1016/j.colcom.2021.100532.
[69] P. Karthik, V. Vinesh, A.R. Mahammed Shaheer, B. Neppolian, Self-doping of Ti3+ in TiO2 through incomplete hydrolysis of titanium (IV) isopropoxide: An efficient visible light sonophotocatalyst for organic pollutants degradation, Appl. Catal. A 585 (2019), 117208, https://doi.org/10.1016/j.apcata.2019.117208.
[70] P.Y. Motlagh, S. Akay, B. Kayan, A. Khataee, Ultrasonic assisted photocatalytic process for degradation of ciprofloxacin using TiO2-Pd nanocomposite immobilized on pumice stone, J. Ind. Eng. Chem. 104 (2021) 582–591, https://doi.org/10.1016/j.jiec.2021.09.007.
[71] M. Preeyanghaa, V. Vinesh, P. Sabarikirishwaran, A. Rajkamal, M. Ashokkumar, B. Neppolian, Investigating the role of ultrasound in improving the photocatalytic ability of CQD decorated boron-doped g-C3N4 for tetracycline degradation and first-principles study of nitrogen-vacancy formation, Carbon n. y. 192 (2022) 405–417, https://doi.org/10.1016/j.carbon.2022.03.011.
[72] A. Reheman, K. Kadeer, K. Okitsu, M. Halidan, Y. Tursun, T. Dilinuer, A. Abulikemu, Facile photo-ultrasonic assisted reduction for preparation of rGO/Ag2CO3 nanocomposites with enhanced photocatalytic oxidation activity for tetracycline, Ultrason. Sonochem. 51 (2019) 166–177, https://doi.org/10.1016/j.ultsonch.2018.10.030.
[73] Z. He, Y. He, F. Chang, Z. Li, J. Niu, M. Li, S. Zhang, X. Li, R. Shi, G. Hu, Efficient pH-universal degradation of antibiotic tetracycline via Co2P decorated Neosinocalamus affinis biochar, Chemosphere 286 (2022), 131759, https://doi.org/10.1016/j.chemosphere.2021.131759.
[74] K. Saravanakumar, A. Fayyaz, S. Park, Y. Yoon, Y.M. Kim, C.M. Park, Hierarchical CoTiO3 microrods on Ti3C2Tx MXene heterostructure as an efficient sonocatalyst for bisphenol A degradation, J. Mol. Liq. 344 (2021), 117740, https://doi.org/10.1016/j.molliq.2021.117740.
[75] Z. Huang, J. Wang, M.-Q. Yang, Q. Qian, X.-P. Liu, L. Xiao, H. Xue, Construction of TiO2-Eggshell for Efficient Degradation of Tetracycline Hydrochloride: Sunlight Induced In-Situ Formation of Carbonate Radical, Materials (basel). 14 (2021) 1598, https://doi.org/10.3390/ma14071598.
[76] S.S. G. C., K. Alkanad, G. Alnaggar, N. Al-Zaqri, M.A. Bajiri, T. B., M.D. Dhileepan, B. Neppolian, L.N. K., Surface defect-engineered CeO 2− x by ultrasound treatment for superior photocatalytic H 2 production and water treatment, Catal. Sci. Technol. 12 (2022) 2071–2083. https://doi.org/10.1039/D1CY01940F.
[77] T.R. Naveen Kumar, P. Karthik, B. Neppolian, Polaron and bipolaron induced charge carrier transportation for enhanced photocatalytic H 2 production, Nanoscale 12 (2020) 14213–14221, https://doi.org/10.1039/D0NR02950E.
[78] T. Ma, Z. Li, G. Wang, J. Zhang, Z. Wang, Efficient Visible-Light Driven Photocatalytic Hydrogen Production by Z-Scheme ZnWO4/Mn0.5Cd0.5S Nanocomposite without Precious Metal Cocatalyst, Catalysts 12 (2022) 1527, https://doi.org/10.3390/catal12121527.
[79] L. Liu, J. Huang, H. Yu, J. Wan, L. Liu, K. Yi, W. Zhang, C. Zhang, Construction of MoO3 nanopaticles /g-C3N4 nanosheets 0D/2D heterojuntion photocatalysts for enhanced photocatalytic degradation of antibiotic pollutant, Chemosphere 282 (2021), 131049, https://doi.org/10.1016/j.chemosphere.2021.131049.
[80] M. Rajamani, K. Rajendrakumar, Chitosan-boehmite desiccant composite as a promising adsorbent towards heavy metal removal, J. Environ. Manage. 244 (2019) 257–264, https://doi.org/10.1016/j.jenvman.2019.05.056.
[81] I. Rapti, T. Kourkouta, E.-M. Malisova, T. Albanis, I. Konstantinou, Photocatalytic Degradation of Inherent Pharmaceutical Concentration Levels in Real Hospital WWTP Effluents Using g-C3N4 Catalyst on CPC Pilot Scale Reactor, Molecules 28 (2023) 1170, https://doi.org/10.3390/molecules28031170.
[82] D.T. Ruziwa, A.E. Oluwalana, M. Mupa, L. Meili, R. Selvasembian, M.M. Nindi, M. Sillanpaa, W. Gwenzi, N. Chaukura, Pharmaceuticals in wastewater and their photocatalytic degradation using nano-enabled photocatalysts, J. Water Process Eng. 54 (2023), 103880, https://doi.org/10.1016/j.jwpe.2023.103880.